bioRxiv preprint doi: https://doi.org/10.1101/748988; this version posted April 17, 2021. The copyright holder for this preprint (which was not certified by peer review) is the author/funder, who has granted bioRxiv a license to display the preprint in perpetuity. It is made available under aCC-BY-NC-ND 4.0 International license.

Diversity amongst human cortical pyramidal neurons revealed via their sag currents and frequency preferences

Homeira Moradi Chameh[1], Scott Rich[1], Lihua Wang[1], Fu-Der Chen[2,3], Liang Zhang[1,4], Peter L. Carlen[1,4,5], Shreejoy J. Tripathy[6,7,8†], Taufik A. Valiante[1,2,5,7,9*†]

[1]Krembil Brain Institute, University Health Network, 60 Leonard Street, Toronto, ON, Canada, M5T 2S8. [2]Department of Electrical and Computer Engineering, University of Toronto, 10 king's College Road, Toronto, ON, Canada, M5S 3G8. [3]Max Planck Institute of Microstructure Physics, Weinberg 2, 06120, Halle, Germany. [4]Departments of Medicine & Physiology, Medical Science Building, University of Toronto, 1 King's College Circle, Toronto, ON, Canada, M5S 1A8. [5]Institute of Biomedical Engineering, Rosebrugh Building, University of Toronto, 164 College Street, Toronto, ON, Canada, M5S 3G9. [6]Krembil Centre for Neuroinformatics, Centre for Addiction and Mental Health, 250 College Street, Toronto, ON, Canada, M5T 1R8. [7]Institute of Medical Sciences, Medical Science Building, University of Toronto, 1 King's College Circle, Toronto, ON, Canada, M5S 1A8. [8]Department of Psychiatry, University of Toronto, 250 College Street, Toronto, ON, Canada, M5T 1R8. [9]Department of Surgery, Division of Neurosurgery, Stewart Building, University of Toronto, 149 College Street, Toronto, ON, Canada, M5T 1P5.

[†]These authors contributed equally.

* taufik.valiante@uhn.ca

Abstract

In the human neocortex coherent interlaminar theta oscillations are driven by deep cortical layers, suggesting neurons in these layers exhibit distinct electrophysiological properties. To characterize this potential distinctiveness, we use in vitro whole-cell recordings from cortical layers 2 and 3 (L2&3), layer 3c (L3c) and layer 5 (L5) of the human cortex. Across all layers we observe notable heterogeneity, indicating human cortical pyramidal neurons are an electrophysiologically diverse population. L5 pyramidal cells are the most excitable of these neurons and exhibit the most prominent sag current (abolished by blockade of the hyperpolarization activated cation current, I_h). While subthreshold resonance is more common in L3c and L5, we rarely observe this resonance at frequencies greater than 2Hz. However, the frequency dependent gain of L5 neurons reveals they are most adept at tracking both delta and theta frequency inputs, a unique feature that may indirectly be important for the generation of cortical theta oscillations.

Introduction

Comparative studies between human and rodent cortical neuronal physiology have revealed unique human cortical neuronal and microcircuit properties. At the cellular level, human neurons have been shown to have unique morphological properties [1], potentially reduced membrane capacitances [2], increased dendritic compartmentalization in thick-tufted L5 pyramidal cells [3], higher h-channel densities in L3 versus L2 pyramidal cells [4], and a wholly unique neuronal cell type [5,6]. At the microcircuit level, human neocortical circuits demonstrate unique reverberant activity [7], different spike-timing dependent plasticity (STDP) rules compared to neocortical circuits in rodents [8], and coherent oscillations between superficial and deep cortical layers [9]. In addition, correlations between patient intelligence quotient (IQ) and cellular features of human layer 2, 3 and 4 pyramidal cells have been demonstrated in both action potential kinetics and the length and complexity of dendritic arbors [10].

bioRxiv preprint doi: https://doi.org/10.1101/748988; this version posted April 17, 2021. The copyright holder for this preprint (which was not certified by peer review) is the author/funder, who has granted bioRxiv a license to display the preprint in perpetuity. It is made available under aCC-BY-NC-ND 4.0 International license.

Although understanding the unique biophysical and synaptic properties of neurons experimentally remains an important endeavor, computational models and mathematical formulations of neurons and circuits are essential for describing and explaining mesoscopic level collective dynamics such as oscillations [11-13]. Indeed, it has been recently posited that "a set of brain simulators based on neuron models at different levels of biological detail" are needed in order to "allow for systematic refinement of candidate network models by comparison with experiments"[14]. By extension, to create simulations of the human brain and cortical microcircuit, we need neuronal models derived from direct human experiments. Thus, as we explore what is uniquely human about the human brain in order to, for example, tackle the increasing societal burden of neurological and neuropsychiatric conditions [15,16], infusing computational models with human derived micro- and mesoscopic cellular and circuit properties will be critically important.

In this context, our previous experiments in human cortical slices have demonstrated that spontaneous theta-like activity, the most ubiquitous oscillation in the human brain [17] can be induced by application of cholinergic and glutamatergic agonists [9]. We observed theta oscillations that were coherent between cortical laminae, with the deep layer leading in phase relative to the superficial layer [9]. We also observed robust cross-frequency coupling between theta and high-gamma activity that was modulated with the strength of synchrony between cortical laminae [18]– "so called coordination though coherent phase–amplitude coupling"[19]. Given the role of intrinsic electrophysiological properties in the generation of oscillations [20] and the finding that deep layer theta leads superficial layer theta in phase, we reasoned that deep layer neurons in the human neocortex are likely endowed with distinct biophysical properties that enable them to "drive" such interlaminar activity.

One of the candidate membrane currents thought to contribute to low-frequency (<8Hz) oscillations is the hyperpolarization activated cation current or h-current (I_h) [3,4,21,22]. This current is important for oscillations and pacemaking activity in a myriad of cell types, ranging from midbrain and hippocampal neurons to cardiac pacemaker neurons [23-25]. Consistent with its role in contributing to resonant activity, a recent study in the human neocortex demonstrated that I_h appeared necessary for the subthreshold resonance observed in L3 neurons [4]. In addition, it has been reported that thick-tufted neurons in L5 of the human neocortex also display prominent somatic and dendritic I_h and subthreshold resonance [3]. However, recent transcriptomic evidence and detailed comparisons to homologous cells in rodents [26] have suggested that these thick-tufted, extra-telencephalic (ET) neurons are much rarer, implying our understanding of the electrophysiological properties of L5 pyramidal neurons remains incomplete.

Based on our previous findings that deep layer activity appears to drive superficial activity in the human cortex [9], we hypothesized that this "leading" role in generating interlaminar coherence can be attributed in part to the differing intrinsic properties of deep layer from superficial layer neurons. In pursuit of this hypothesis, we sought to gain a more complete understanding of the features of human L5 cortical pyramidal neurons. We used whole-cell recordings to characterize pyramidal cells in L2&3, L3c, and L5, focusing on the amplitude and kinetics of I_h via the sag voltage. In addition to key biophysical differences favoring greater excitability in human L5 versus L2&3 pyramidal cells, we found that L5 and L3c demonstrated larger sag voltage amplitudes relative to L2&3 pyramidal cells generally. Somewhat surprisingly, while some subthreshold resonance at >2Hz was observed in our experiments, we found this feature to be generally quite rare amongst pyramidal cells across all layers. However, we did find that L5 pyramidal cells showed enhanced frequency dependent gain at delta and theta frequencies, which motivates our presentation of a "dynamic circuit motif" [20] underlying how L5 neurons "drive" human cortical theta. Lastly, we found notable cell-to-cell variability in electrophysiological parameters sampled from pyramidal cells recorded within the same lamina consistent with previous studies in human L2&3 [4,27,28], and further reveal that this variability is especially large in L5.

bioRxiv preprint doi: https://doi.org/10.1101/748988; this version posted April 17, 2021. The copyright holder for this preprint (which was not certified by peer review) is the author/funder, who has granted bioRxiv a license to display the preprint in perpetuity. It is made available under aCC-BY-NC-ND 4.0 International license.

Table 1: Demographic data (for a subset of 49 patients where such information was available)

Age (Years)	Sex	Years of seizure history	Diagnosis	Antiepileptic drugs	Resection location
39	F	11	Tumor	LSC, LRZ, LEV	Right-ATL
58	F	8	Tumor	CBZ	Left-FL
57	M	45	Epilepsy	LSC, CZP, CBZ	Right-ATL
27	M	11	Epilepsy	LSC, LRZ, CLB	Right-ATL
24	M	8	Epilepsy	LEV, LTG	Right-ATL
25	M	12	Epilepsy	CBZ, LSC	Right-ATL
33	F	4	Epilepsy	LEV	Left-FL
33	M	14	Epilepsy	PHN, LEV	Right-FL
22	M	6	Epilepsy	PHN, CBZ, LTG	Left-ATL
21	M	2	Epilepsy	DR, CLB, MJ	Left Parietal lobe
22	M	12	Epilepsy	PHN, LRZ	Right-ATL
23	F	23	Epilepsy	CBZ, LEV, LSC	Right-FL
53	F	43	Epilepsy	CBZ, LSC, LEV	Left-ATL
37	F	2	Tumor	GPN, LSC, LEV, CLB, LRZ	Right-FL
47	F	4	Epilepsy	CBZ, CLB	Left-ATL
52	M	13	Epilepsy	CBZ, CLB	Left-ATL
50	F	26	Epilepsy	PHN, LTG	Right-ATL
36	F	34	Epilepsy	LSC, CBZ	Left-ATL
40	M	29	Epilepsy	LEV	Right-ATL
25	F	10	Epilepsy	CBZ, LSC, LEV	Right-ATL
52	M	27	Epilepsy	LSC, LRZ	Left-ATL
21	M	11	Epilepsy	LTG, CBZ	Left-ATL
63	M	0.1	Tumor	PHN	Right-Parietal lobe
42	M	22	Epilepsy	CBZ	Right-FL
25	F	22	Epilepsy	LSC, CLB, LTG	Right-FL
24	F	3	Tumor	LEV	Left-ATL
53	M	9	Epilepsy	LEV	Left-ATL
45	F	20	Epilepsy	LTG	Right-ATL
26	F	25	Epilepsy	CBZ, CLB, LTG	Right-ATL
35	F	14	Epilepsy	LRZ, DR, PHN	Left-ATL
24	M	6	Epilepsy	LSC, LRZ, MJ	Right-ATL
53	F	51	Epilepsy	LSC, CLB	Left-ATL
44	F	3	Epilepsy	LTG	Left-ATL
25	M	14	Epilepsy	CBZ	Right-ATL
19	F	15	Epilepsy	PB, CLB, GPN, RFM	Right-ATL
30	M	12	Epilepsy	PHN	Left-ATL
26	M	5	Epilepsy	CBZ, DR	Right-ATL
28	M	13	Epilepsy	CLB, MJ	Left-ATL
52	F	6	Epilepsy	LTG, LEF	Left-ATL
26	F	9	Epilepsy	ESL, TMP, CLB	Right-ATL
59	F	39	Epilepsy	CLB, LSC	Right-ATL
37	M	5	Epilepsy	CLB, LSC	Right-ATL
55	M	27	Epilepsy	CLB, ESL, LTG	Left-ATL
42	F	3	Epilepsy	CBZ, GPN	Right-ATL
57	F	56	Epilepsy	CLB, LTG, PRM, CBD oil	Left-ATL
24	M	4	Epilepsy	LEV, LTG	Left ATL
33	M	6	Epilepsy	LSC, PGBPHN	Right-ATL
39	M	12	Epilepsy	CLB, LTG, MJ	Left-ATL
36	F	16	Epilepsy	LSC, PGB, PHN	Right-ATL

CBZ, Carbamazepine; CLB, Clobazam; CZP, Clonazepam; DR, Divalproex; GPN, Gabapentin; LEV, Levetiracetam; LRZ, Lorazepam; LSC, Lacosamide; LTG, Lamotrigine; MJ, Marijuana; PB, Phenobarbital; PHN, Phenytoin; RFM, Rufinamide; LEF, Leflunomide; ESL, Eslicarbazepine Acetate; TMP, Tetramethylpyrazine; PRM, primidone; CBD, cannabidiol; PGB, Pregabalin; FL, Frontal lobe.

bioRxiv preprint doi: https://doi.org/10.1101/748988; this version posted April 17, 2021. The copyright holder for this preprint (which was not certified by peer review) is the author/funder, who has granted bioRxiv a license to display the preprint in perpetuity. It is made available under aCC-BY-NC-ND 4.0 International license.

Results

Whole-cell patch clamp recordings were obtained from human neocortical neurons located in L2&3, L3c and L5 within acute brain slices collected from 61 patients. Tissues were obtained primarily from patients who underwent resective surgery for pharmacologically intractable epilepsy (see Table 1 for a summary of patient details). For many of our recordings, we did not annotate our L2&3 pyramidal cells as specifically belonging to either L2 or L3 considering the majority of these data were collected prior to publication of a recent paper illustrating divergent electrophysiological and morphological features of these neurons in the human neocortex [4]. Consequently, we later recorded from a targeted set of pyramidal cells in L3c (i.e., the deepest part of L3) to specifically contrast and compare our findings with those from previous findings [4].

Diverse morphologies and passive membrane properties of pyramidal cells in L2&3, L3c and L5

To confirm the successful targeting of pyramidal cells, a subset of neurons were filled with biocytin and underwent subsequent morphological reconstruction. Figure 1a shows example electrophysiological sweeps of L2&3, L3c and L5 pyramidal cells with corresponding 3D morphological reconstructions.

The 3D reconstructions revealed a rich diversity of human pyramidal cell morphologies, consistent with recent detailed demonstrations of the distinct cellular morphologies of human cortical neurons as a function of cortical lamina [1,3,4,27]. Pyramidal cells with somas located in L2 and the upper part of L3 had complex basal dendrites, with apical dendrites often reaching L1. Pyramidal cells located in L3c showed different morphologies, with one cell (cell d) showing simple basal dendrites and another (cell e) showing much more complex basal dendrites, consistent with recent reports on the heterogeneity of pyramidal cells in L3 [27]. Lastly, we observed two L5 neurons with very different morphologies: one cell (cell f) displays a simple morphology with apical dendrites terminating at the border of L3 and L4, and another, considerably larger pyramidal cell (cell g) with a highly complex basal dendrite and two apical dendrite trunks, with one trunk terminating in upper L3 and the other projecting to lower L3 prior to its abrupt termination due to slicing or optical truncation.

While we note that our human L5 morphologies are different from those reported by Beaulieu-Laroche et al. [3] that targeted rare thick-tufted L5 pyramidal cells [26] with tufts reaching into L1 [29], our cell morphologies are consistent with other previous reports that relatively few L5 neurons have dendrites extending past L3 [1]. Additionally, given the challenge of potential dendrite truncation when preparing slices containing such large cells [1], it is possible that our representative L5 morphologies in Figure 1 have been inadvertently truncated [1]. However, we only observed visible truncation in one branch of one cell (the largest cell, cell g) and no obvious truncation in the other cells shown in Figure 1.

We next assessed the passive membrane properties (i.e. resting membrane potential, input resistance and membrane time constant) of human cortical pyramidal cells in L2&3, L3c and L5 (n=56, n=15 and n=105 neurons, respectively) using hyperpolarizing current steps in current-clamp mode (see Methods). We found that passive membrane properties differed significantly between pyramidal cells of L2&3, L3c and L5. Additionally, we found that L3c and L5 neurons had more depolarized resting membrane potentials relative to L2&3 neurons (L2&3: -68.2 ± 5.3 mV, L3c: -65.6 ± 3.8 mV, L5: -65.6 ± 6.5mV; Fig. 1b), with L5 neurons being significantly more depolarized at rest compared to L2&3 neurons (p=0.007). We also found that L5 pyramidal cells showed higher input resistances relative to L2&3 and L3c neurons (L2&3: 83± 38.1 MΩ, L3c:79.4 ± 21.4 MΩ, L5: 94.2 ± 41.3 MΩ; Fig. 1c). This difference was not significant between layers (p=0.110). L5 and L3c pyramidal cells also had slower membrane time constants (τ_m) compared to L2&3 (L2&3: 13.7 ± 7.1 ms, L3c: 17.1 ± 5.7 ms, L5: 19.3 ± 9.1 ms, p<0.0001; Fig. 1d).

bioRxiv preprint doi: https://doi.org/10.1101/748988; this version posted April 17, 2021. The copyright holder for this preprint (which was not certified by peer review) is the author/funder, who has granted bioRxiv a license to display the preprint in perpetuity. It is made available under aCC-BY-NC-ND 4.0 International license.

In general, we found considerable electrophysiological heterogeneity among neurons sampled within each cortical layer, broadly consistent with the morphological reconstructions shown in Figure 1a. For example, we found that pyramidal cells in L5 had input resistances as low as 20 MΩ and as high as 200 MΩ, possibly reflecting the dichotomy between thin- and thick-tufted pyramidal cells and/or the graded variation between pyramidal cells of varying sizes and dendritic complexities (as well as the potential inadvertent cutting of dendrites during slice preparation, see Discussion).

We further compared these findings to published and publicly available datasets from human pyramidal cells. We note that the average input resistance among our population of recorded L5 pyramidal cells is considerably higher than that reported in Beaulieu-Laroche et al. [3], most likely due to differences in the neurons targeted for recordings between our studies. We also made use of a publicly-accessible dataset of 272 pyramidal cells sampled from L2, L3, and L5 from an additional cohort of 39 human surgical patients characterized by the Allen Institute for Brain Sciences (http://celltypes.brain-map.org/). We note that while the overall experimental design of the Allen Institute's dataset is similar to ours, there are some methodological differences, such as the composition of solutions used for slice preparation and recording (see Methods). The Allen Institute data are generally consistent with our finding that input resistances in L5 pyramidal cells are not smaller than those sampled in human L2 and L3 (Supplementary Fig 1a) and that this trend holds even in neurons where the primary dendrites are not visibly truncated (Supplementary Fig. 1b). We further note that, while it appears L5 neurons have increased variability in these intrinsic properties relative to L2&3, the levels of heterogeneity are consistent with prior reports from L2&3 in previous human studies [4,27,28].

bioRxiv preprint doi: https://doi.org/10.1101/748988; this version posted April 17, 2021. The copyright holder for this preprint (which was not certified by peer review) is the author/funder, who has granted bioRxiv a license to display the preprint in perpetuity. It is made available under aCC-BY-NC-ND 4.0 International license.

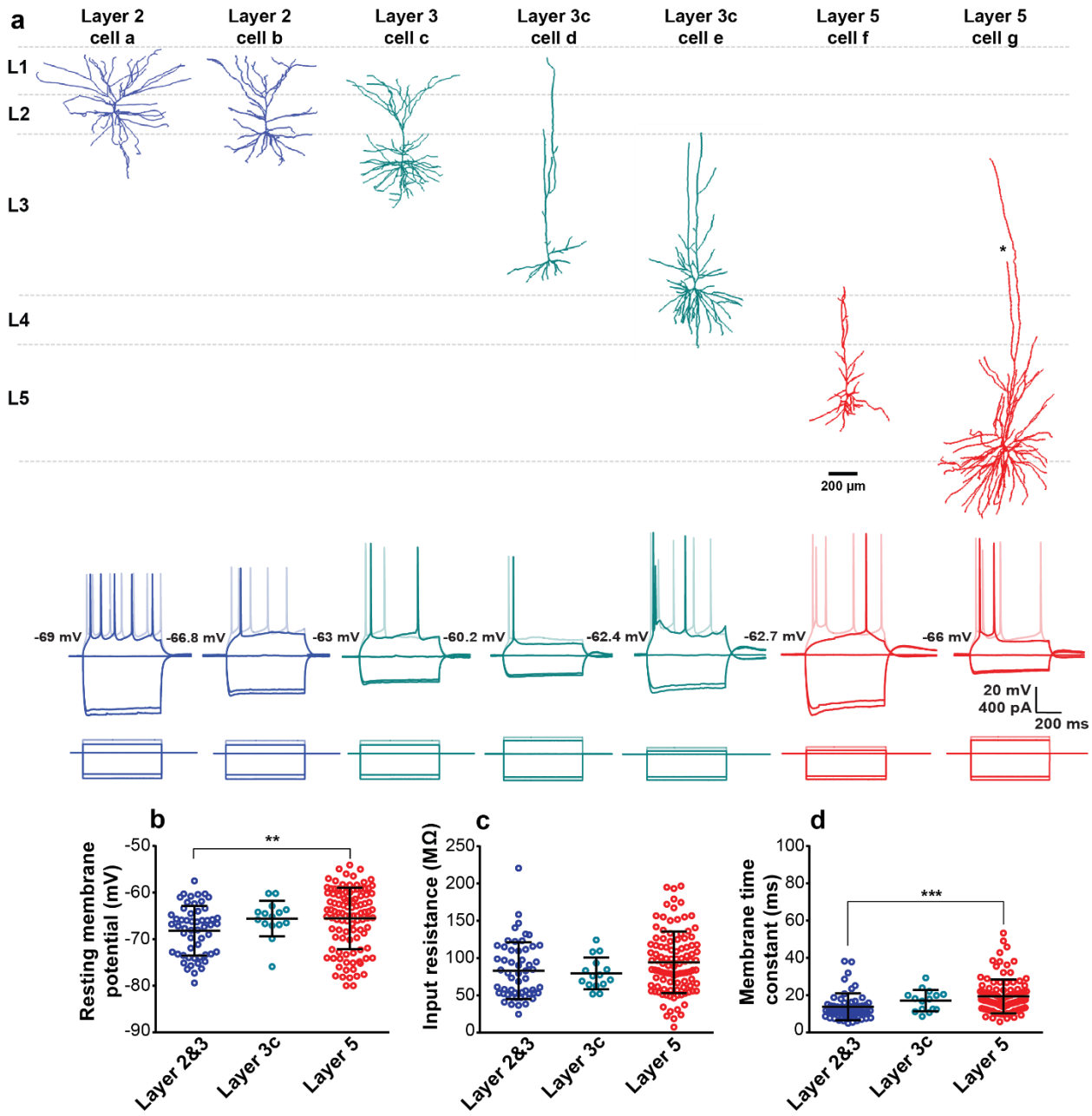

Figure 1. Diverse morphologies and passive membrane properties among pyramidal cells in the human neocortex. a Example 3D reconstructions (top) and voltage traces (bottom) for L2&3, L3c and L5 pyramidal cells following hyperpolarizing and depolarizing current injection. Cortical layer and relative position from pial surface are annotated for each reconstructed cell. Asterisk in one branch of apical dendrite in cell g with truncation (dendrite morphologies were otherwise not visibly truncated). **b, c, d** Resting membrane potentials (p=0.007) (b), input resistances (p=0.111) (c) and membrane time constants (p<0.001) (d) for pyramidal cells in L2&3, L3c, and L5. Error bars in b-d denote mean and standard deviations (SD). One-Way ANOVA post hoc with Dunn's multiple comparison test were used for statistical comparison. L2&3 (n=56), L3c (n=15) and L5 (n=105). Source data are provided as a Source Data file.

bioRxiv preprint doi: https://doi.org/10.1101/748988; this version posted April 17, 2021. The copyright holder for this preprint (which was not certified by peer review) is the author/funder, who has granted bioRxiv a license to display the preprint in perpetuity. It is made available under aCC-BY-NC-ND 4.0 International license.

Subthreshold active membrane properties of pyramidal cells in L2&3, L3c and L5

To assay sag voltage and rebound depolarization we injected a series of hyperpolarizing currents (L2&3: n=56, L3c: n=15, L5: n=105). L5 pyramidal cells had significantly larger sag voltage amplitudes than L2&3 pyramidal cells (L2&3: 1.7 ± 1.1 mV, L3c: 2.3 ± 0.7 mV, L5: 3.2 ± 1.9 mV, p<0.0001 between L2&3 and L5; Fig. 2a, b). We found similar results using the dimensionless sag ratio measure that normalizes for input resistance differences between neurons (Supplementary Fig. 2a). We note that sag ratio is positively correlated with sag amplitudes (Supplementary Fig. 3, r=0.68). These results were further replicated from the Allen Institute dataset (Supplementary Fig. 4; L2: 0.51 ± 0.045; L3: 0.125 ± 0.067; L5: 0.149 ± 0.072; p = 2.21 x 10^{-6} between L2 and L3, p=0.012 between L3 and L5). These findings support recent evidence for a positive correlation between sag voltage amplitude and distance from pial surface [4] with our results further extending this relationship to L5.

In addition, 21.9% of L5 neurons exhibited rebound spiking following the termination of a hyperpolarizing current pulse, whereas 1.8% of L2&3 neurons exhibited rebound spiking, and rebound spiking was not observed in L3c neurons. The rebound depolarization amplitude was significantly larger in L5 pyramidal cells compared to L2&3 and L3c neurons (L2&3: 1.8 ± 1. 6mV, L3c: 2.9 ± 1.8, L5: 4.2 ± 3 mV, p<0.001 between L2&3 and L5; Fig. 2c).

To further characterize the I_h specific component of membrane sag voltage we bath applied the specific I_h blocker ZD7288 (10 µm; ZD), with example traces shown in Figure 2d. For L2&3 (n=13), L3c (n=4) and L5 (n=10) pyramidal cells, after bath applying ZD we observed a significant reduction in voltage sag amplitude (L2&3: before 1.3 ± 0.9 mV, after 0.2 ± 0.3 mV, p=0.001, L3c: before 2.4 ± 1.4 mV, after 0.9 ± 0.9 mV, P=0.100, L5: before 3.1 ± 2.8 mV, after 0.9 ± 0.8 mV, p=0.002; Fig. 2e) and in sag ratio (Supplementary Fig. 2b). Bath applying ZD7288 also significantly reduced the rebound depolarization amplitude (L2&3: before 1.3 ± 1.1 mV, after -0.8 ± 1.5 mV, p=0.001, L3c: before 3 ± 2.3 mV, after 0.9 ± 1.6 mV, p=0.100, L5: before 2.1 ± 1.9 mV, after -1.2 ± 2.3 mV, p=0.002; Fig. 2f).

Voltage-clamp experiments were performed in a subset of neurons (L2&3: n=6, L5: n=10) to determine if the I_h amplitude differences arose from differences in channel kinetics between these two cell-types. While space-clamp issues limit our ability to adequately voltage clamp distal cellular processes [30], we nevertheless considered it beneficial to use this technique to obtain semi-quantitative estimates of the amplitudes, kinetics, and voltage dependence of I_h in human pyramidal cells. We used pharmacological blockers to specifically isolate I_h (see Methods). We found that injecting voltage steps from -60 to -140mV produced a slowly activating inward current (example traces shown in Supplementary Fig. 5a). Consistent with our current clamp results, we found that the amplitudes of the I_h were significantly smaller in L2&3 neurons compared with L5 (Supplementary Fig. 5c), whereas the time course of I_h activation and the voltage sensitivity of I_h (quantified at the half maximal activation voltage) was similar between L2&3 and L5 neurons (Supplementary Fig. 5b and d). These results suggest that the relatively larger L5 sag amplitude arises from increased channel numbers rather than differences in channel kinetics.

bioRxiv preprint doi: https://doi.org/10.1101/748988; this version posted April 17, 2021. The copyright holder for this preprint (which was not certified by peer review) is the author/funder, who has granted bioRxiv a license to display the preprint in perpetuity. It is made available under aCC-BY-NC-ND 4.0 International license.

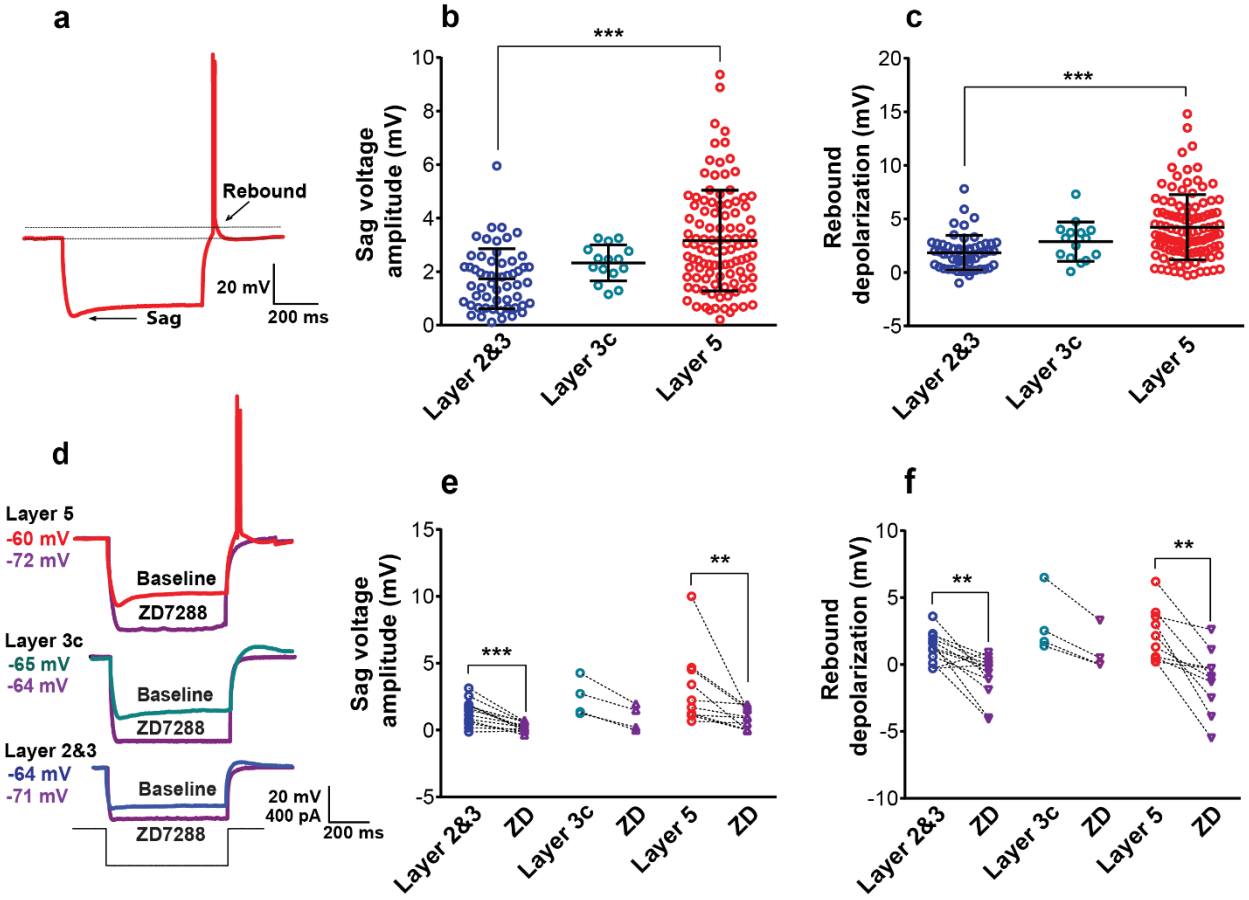

Figure 2. I_h related membrane properties are more apparent in L5 pyramidal cells compared to L2&3 and L3c. a Example voltage sweep from a representative L5 pyramidal cell during injection of -400 pA hyperpolarizing current step. Arrows indicate sag voltage and rebound depolarization and post-hyperpolarization rebound spiking. **b, c** Sag voltage amplitude (p<0.0001; One-Way ANOVA post hoc with Dunn's multiple comparison test, L2&3 (n=56), L3c (n=15) and L5 (n=105)). (b) and rebound depolarization amplitude (p<0.0001; One-Way ANOVA post hoc with Dunn's multiple comparison test, L2&3 (n=56), L3c (n=15) and L5 (n=105)). (c) among sampled L2&3, L3c, and L5 pyramidal cells in response to injection of hyperpolarizing current. Lines and error bars denote mean and SD and asterisks indicate significance of group comparison. **d** Example of voltage sweeps at baseline (red, green, and blue) and after (purple) bath application of the I_h blocker ZD7288 (10 µM) following injection of -400 pA. **e, f** Bath application of ZD7288 diminished sag voltage amplitude (L2&3-ZD: p=0.001, n=13; L3c-ZD: p=0.125, n=4; L5-ZD: p=0.002, n=10; Wilcoxon matched-pairs signed rank test) (e) and rebound depolarization amplitude (L2&3-ZD: p=0.002, n=13; L3c-ZD: p=0.125, n=4; L5-ZD: p=0.002, n=10; Wilcoxon matched-pairs signed rank test) (f) in all layers. Source data are provided as a Source Data file.

Suprathreshold active membrane properties of pyramidal cells in layers 2/3, L3c and 5

Active membrane property differences between layers were characterized by examining the firing patterns of L2&3, L3c and L5 human pyramidal cells (n=55, n=15, n=104 neurons respectively) using a series of depolarizing current pulses (0-400 pA, 600ms) with examples shown in Figure 3a-c. L5 neurons had a significantly larger action potential than L2&3 neurons (L2&3: 81.9 ± 13.2 mV, L3c: 88.3 ± 7.5 mV, L5: 88.7

bioRxiv preprint doi: https://doi.org/10.1101/748988; this version posted April 17, 2021. The copyright holder for this preprint (which was not certified by peer review) is the author/funder, who has granted bioRxiv a license to display the preprint in perpetuity. It is made available under aCC-BY-NC-ND 4.0 International license.

± 18.2 mV, p=0.020; Fig. 3d). In addition, the action potential half-width was similar in L5 compared to L2&3 (L2&3: 1.8 ± 0.6 ms, L5: 1.8 ± 0.7 ms). However, the half-width of the action potential was significantly longer in L3c pyramidal cells compared to L2&3 (p=0.029, L3c: 2.2 ± 0.6 ms) and L5 pyramidal cells (p=0.022, Fig. 3f).

The frequency-current relationships (f-I curve) showed greater f-I slopes for L5 relative to L2&3 and L3c neurons (Fig. 3g; at 300 pA, L2&3: 16.3 ± 12.2 Hz, L3c: 11.0 ± 12.2 Hz, L5: 21.8 ± 13.1 Hz, p=0.003 between L2&3 and L5 neurons, and p=0.001 between L5 and L3c neurons). The current needed to elicit an action potential was significantly lower in L5 neurons compared to L2&3 (L2&3: 162.1 ± 81.9 pA, L3c: 153.5 ± 66.6 pA, L5: 121.1 ± 85.2 pA, p=0.002 between L2&3 and L5; Fig. 3h). We also note that these distributions were especially broad, particularly for L5 pyramidal cells, mirroring the large range in input resistances and diverse morphologies of these neurons (Figure 1). L5 neurons showed significantly less spike frequency adaptation relative to L2&3 and L3c neurons (L2&3: 0.16 ± 0.16, L3c: 0.25 ± 0.16, L5: 0.11 ± 0.13, p=0.010 between L5 and L2&3, p=0.001 between L5 and L3c; Fig. 3i). Lastly, we identified a small number of bursting neurons (defined as those with instantaneous frequencies at rheobase >75Hz) in our dataset (e.g., the L5 cell illustrated in Fig. 3c and further examples in Supplementary Fig. 6). Specifically, we found 14% of our recorded L2&3 pyramidal cells and 9.5% of L5 pyramidal cells showing bursting activity. The overall low number of bursting neurons in both superficial and deeper cortical layers of human neocortex are consistent with previous report of infrequent bursting in human neocortex [3].

bioRxiv preprint doi: https://doi.org/10.1101/748988; this version posted April 17, 2021. The copyright holder for this preprint (which was not certified by peer review) is the author/funder, who has granted bioRxiv a license to display the preprint in perpetuity. It is made available under aCC-BY-NC-ND 4.0 International license.

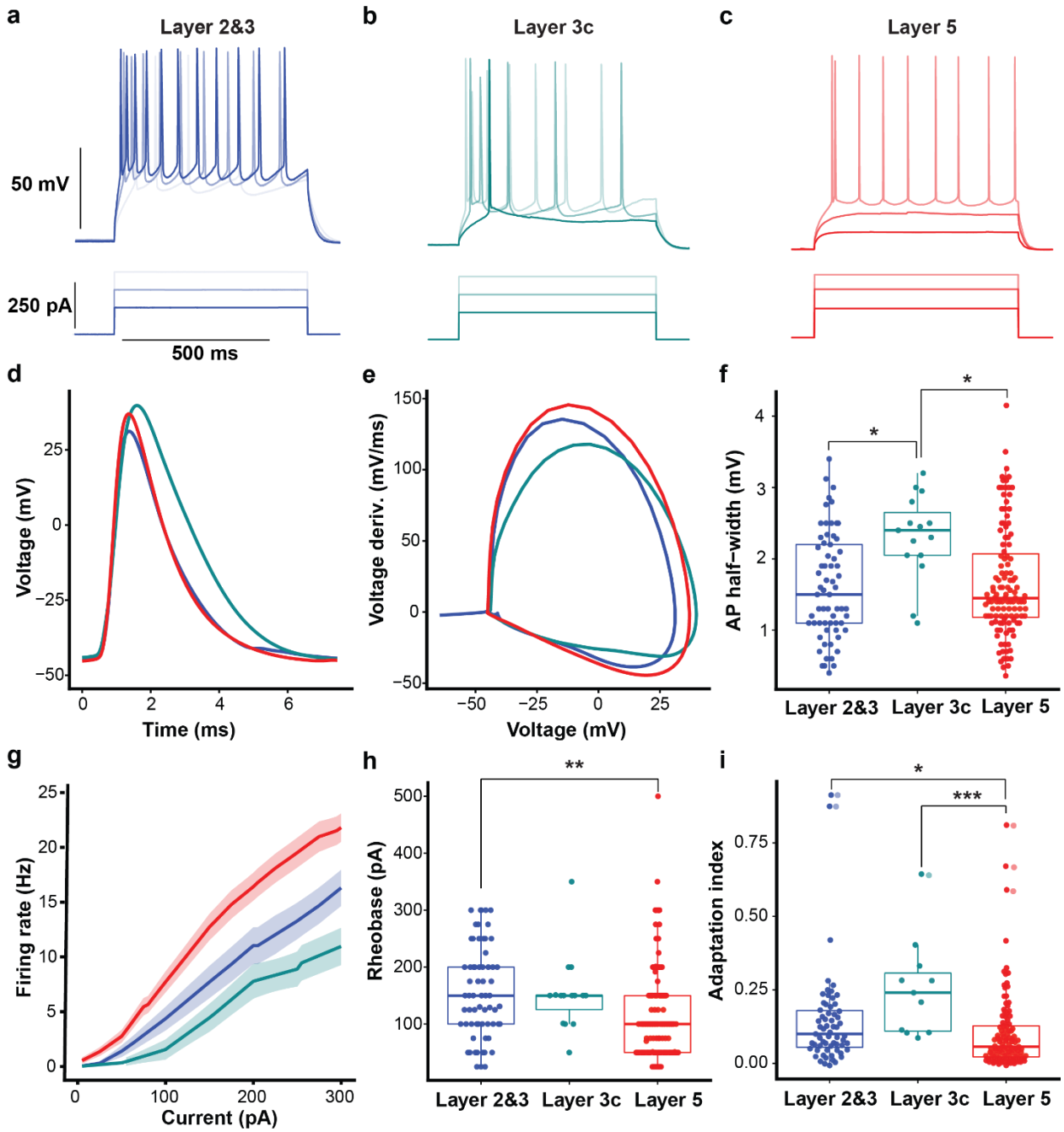

243

244 **Figure 3. L5 pyramidal cells display higher frequency firing rate and less adaptation than L2&3 and L3c**
245 **neurons. a, b, c** Example L2&3, L3c and L5 pyramidal cell voltage responses following depolarizing current
246 injections (150 pA, 250 pA and 300 pA, 600 ms). **d, e** Action potential waveform (d) and action potential
247 phase plot (e) averaged over recorded pyramidal cells in each layer. **f** L5 pyramidal cells had a smaller action
248 potential half-width compared to L2&3 and L3c neurons which was not significant in comparison with L2&3
249 neurons. Half-width of action potential was higher significantly in L3c pyramidal cells compared with L2&3
250 and L5 neurons (p=0.029 between L2&3 and L3c, p=0.022 between L3c & L5). **g** Current versus firing rate
251 relationships (FI curves), averaged over pyramidal cells recorded in each layer. Shaded bands indicate SEM.

bioRxiv preprint doi: https://doi.org/10.1101/748988; this version posted April 17, 2021. The copyright holder for this preprint (which was not certified by peer review) is the author/funder, who has granted bioRxiv a license to display the preprint in perpetuity. It is made available under aCC-BY-NC-ND 4.0 International license.

h L5 pyramidal cells needed less depolarizing current to display first action potential compared to L2&3 and L3c neurons (p=0.002). **i** L5 pyramidal cells show less spike frequency adaption, quantified using the adaptation index measure, in comparison with L2&3 and L3c. (p=0.016 between L2&3 and L5; p=0.001 between L3c and L5). One-Way ANOVA post hoc with Dunn's multiple comparison test were used for statistical comparison L2&3 (n=55), L3c (n=15) and L5 (n=104). Data presented as mean ±SD in panels f, h and i. Boxplots in f, h, I denote interquartile range and whiskers denote data range excluding outliers. Source data are provided as a Source Data file.

Subthreshold and suprathreshold frequency preference in human pyramidal cells across cortical layers

Resonance is a common approach to characterize the frequency preferences of neurons and represents the net result of the interaction between passive and active properties [32]. Indeed, human pyramidal cells, and in particular those in deeper part of L3 as well as thick-tufted neurons in L5, can exhibit low frequency subthreshold resonance [3,4]. These findings in human neurons are consistent with studies in rodent cortex that describe the correlation between a large sag voltage and low frequency resonance [33].

We examined subthreshold resonance in our recorded L2&3, L3c and L5 pyramidal cells using a 20 second long frequency-modulated (or ZAP) current stimulus delivered at the resting membrane potential [21]. Our analysis revealed clear examples of resonant pyramidal cells in each of the three major layers we profiled (Fig. 4a and b) and identified a number of neurons that displayed a non-zero peak in their resonant frequency (fR; 27% of L2&3 neurons; 47% of L3c neurons; and 40% of L5 neurons), but considerably few neurons with resonant frequencies greater than 2Hz (Fig. 4c). We found there was a slight trend of a decrease in the 3dB cutoff frequency in L5 relative to L2&3 neurons (p=0.050, Fig. 4d). These results are generally consistent with recent evidence for greater subthreshold resonance in the deeper part of the supragranular layers of the human neocortex relative to more superficial neurons [4]. While we observed a smaller fraction of resonant cells than previous work, we note that our results correspond with the conclusion that human L2&3 pyramidal cells are most likely to have normalized impedance peaks at <2Hz, while neurons with peaks at >4Hz are quite rare. Possible explanations for the lower fraction of resonant cells in our data include our use of different experimental solutions than Kalmbach et al., as well as the possibility of inadvertent dendrite truncation in these experiments (see Discussion). Additionally, our neurons displayed a slightly more depolarized RMP [4], which is a determinant of observing resonance [31].

We further compared the frequency response characteristics of L2&3 and L5 pyramidal cells in response to suprathreshold ZAP current injections with example traces shown in (Fig. 4e). We found that L5 neurons spike with greater fidelity to higher frequency stimuli (12-18Hz) relative to L2&3. We did not observe a difference in frequency tracking at other frequency ranges (Fig. 4f), including frequencies at delta or theta (1-8Hz). We note that the lack of direct correspondence between our sub- threshold and firing rate resonance properties is not surprising, especially in light of theoretical and computational explorations that reveal the lack of a direct link between sub- and suprathreshold stimuli responses [34-37].

bioRxiv preprint doi: https://doi.org/10.1101/748988; this version posted April 17, 2021. The copyright holder for this preprint (which was not certified by peer review) is the author/funder, who has granted bioRxiv a license to display the preprint in perpetuity. It is made available under aCC-BY-NC-ND 4.0 International license.

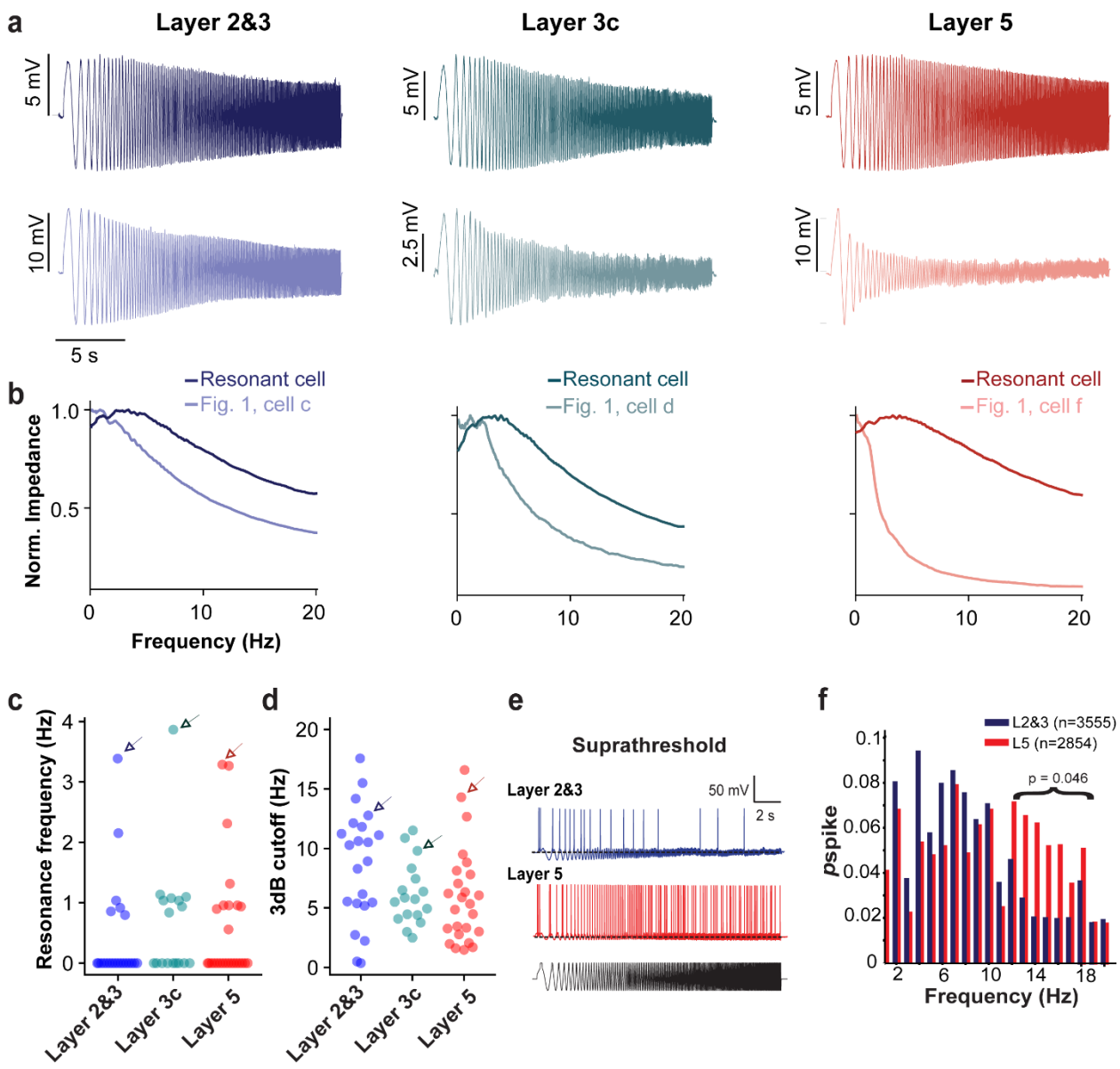

288

289 **Figure 4. Subthreshold and suprathreshold resonance properties of L2&3, L3c and L5 pyramidal cells. a**
290 Example voltage responses following injection of subthreshold frequency-modulated (ZAP) current
291 delivered at resting membrane potential in L2&3, L3c and L5 pyramidal cells. Voltage traces are averaged
292 across 5 repeated trials. Top voltage trace indicates response of a cell displaying subthreshold resonance
293 and bottom trace corresponds to example cell morphologies shown in Figure 1. Cell labels are provided
294 below in b. **b** Normalized impedance profiles for the voltage traces shown in a, with impedances normalized
295 to a maximum value of one. **c,d** Resonance frequencies (c) and 3dB cutoff frequencies (d) indicate that
296 there are relatively few strongly resonant pyramidal cells in our dataset. Arrows in c and d correspond to
297 resonant cells highlighted in a and b. n = 23, 17, 25 cells in L2&3, L3c, L5 respectively. **e** Example voltage
298 responses following injection of suprathreshold ZAP current. **f** Spike response probability in response to
299 suprathreshold current injection shows that L2&3 and L5 pyramidal cells track theta frequencies with
300 greater reliability. The distributions were not significantly different (KS*p*=0.530). Above 12Hz spike

bioRxiv preprint doi: https://doi.org/10.1101/748988; this version posted April 17, 2021. The copyright holder for this preprint (which was not certified by peer review) is the author/funder, who has granted bioRxiv a license to display the preprint in perpetuity. It is made available under aCC-BY-NC-ND 4.0 International license.

probabilities differed significantly between L2&3 and L5 (p=0.046; Two-sample Kolmogorov–Smirnov, L2&3 n=27, L5 n=30). Source data are provided as a Source Data file.

Assessment of frequency-dependent gain reveals greater preference for delta and theta frequencies among L5 relative to L2&3 pyramidal cells

To further investigate the suprathreshold frequency preference of human neurons, a key determinant of their participation in the amplification and/or generation of oscillations [20], we characterized the frequency dependent gain [*G(f)*] and the mean phase shift of the spike response (Fig. 5a) [38] in a subset of neurons (n=8 neurons each for L5 and L2&3) from an additional set of patients (n=5). *G(f)* was quantified via stimulating neurons with multiple trials of a frozen filtered white noise current stimulus. This measure captures distinct neuronal features compared to sub- or suprathreshold resonance: while resonance identifies the likelihood of a spike occurring from a drive at a particular frequency that is itself is suprathreshold, the frequency dependent gain quantifies the phase preference of neuronal spiking as a function of frequency [39] from a noisy input that is relatively small [38]. Neurons with a high gain at a specific frequency are more likely to have a phase preference at that frequency than at other frequencies.

We found that both L2&3 and L5 neurons displayed peaks in *G(f)* within the delta and theta frequency ranges (Fig. 5b). Both peaks were significantly more pronounced in L5 pyramidal cells compared to L2&3 ($p<0.05$). Additionally, above 10Hz, we found that L5 pyramidal cells displayed greater frequency dependent gain than L2&3 neurons, corresponding with the intuition from our suprathreshold ZAP results (Fig. 4f). The greater excitability and fidelity of L5 neurons was also evident in their phase curves and spike triggered averages (STAs) (Fig. 5c and d). L2&3 neurons demonstrated a greater lag in firing than L5 neurons, and their STA were of larger amplitude with steeper slopes. This suggests that L2&3 neurons require larger inputs to trigger spikes, and when they do spike, they will lag behind L5 pyramidal cells if inputs are coincident.

To explore the contribution of I_h to *G(f)* for both L2&3 (n=3, Fig. 5e) and L5 pyramidal cells (n=3, Fig. 5f), ZD7288 (an I_h blocker) was applied to compare *G(f)* before and after abolishing the I_h. We found that blocking I_h predominantly abolished the delta peak in L5 neurons. These data indicate that human L5 pyramidal cells are better at tracking both delta and theta frequency inputs than superficial layer neurons (although L3c neurons were not tested in this way), and our (perhaps preliminary) explorations of the effect of ZD on the frequency dependent gain provides evidence that the larger I_h in L5 pyramidal cells plays an important role in their increased responsiveness to delta frequency inputs.

bioRxiv preprint doi: https://doi.org/10.1101/748988; this version posted April 17, 2021. The copyright holder for this preprint (which was not certified by peer review) is the author/funder, who has granted bioRxiv a license to display the preprint in perpetuity. It is made available under aCC-BY-NC-ND 4.0 International license.

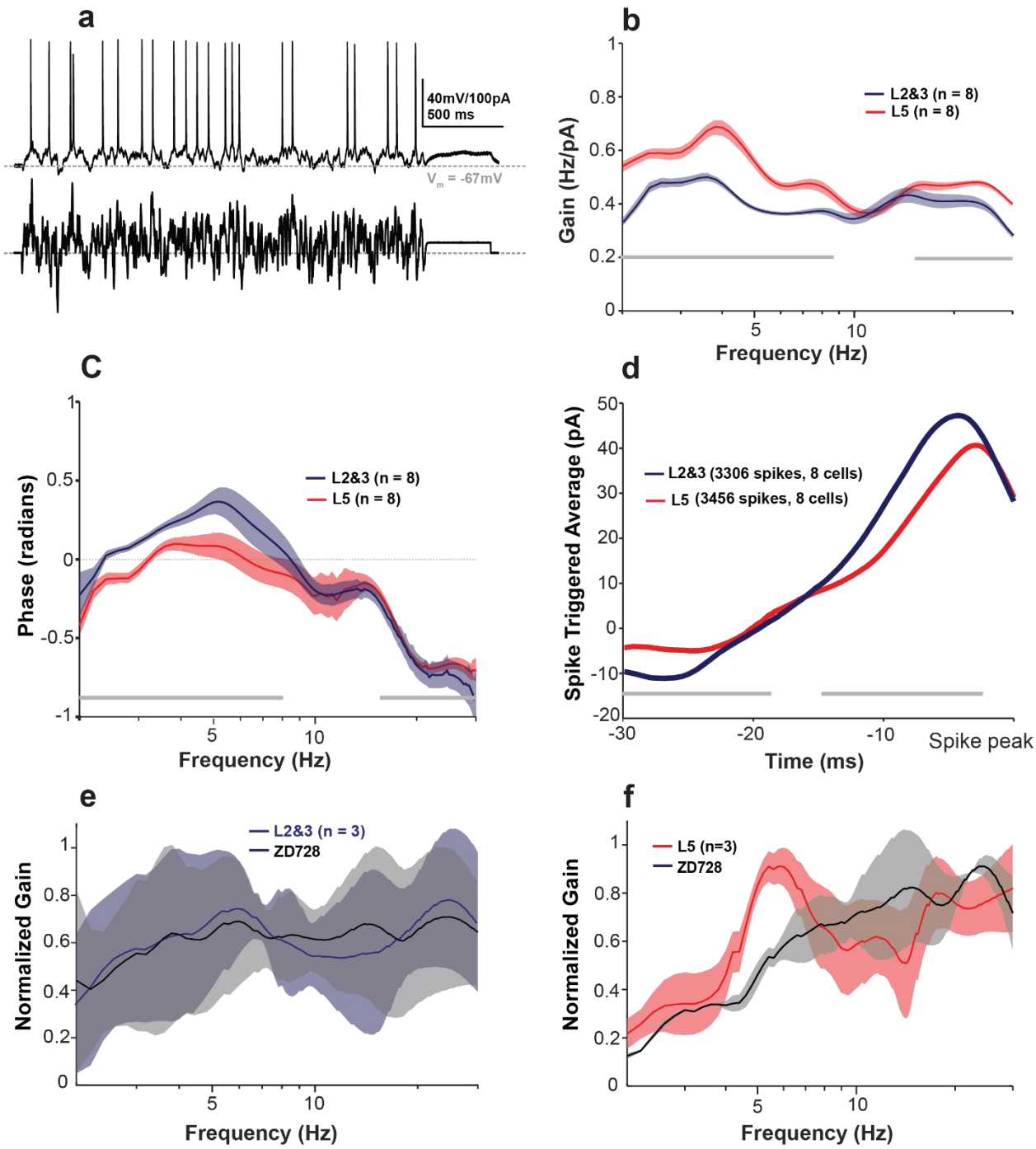

Figure 5: Human L5 neurons display greater gain at delta and theta frequencies than L2&3 pyramidal cells. a Example of V_m response of L5 pyramidal cell to 2.5 seconds of frozen filtered Gaussian white noise current injection. **b** Frequency dependent gain *G(f)* profile of L2&3 and L5 pyramidal cells over a wide range of frequencies. Both layers show two peaks around 2.5-10Hz, and 12-16Hz which are more pronounced in L5 pyramidal cells compared to L2&3. Gray horizontal bars represent significant differences between groups ($p<0.05$; Mann-Whitney U). **c** Phase shift of spiking relative to input stimulus. L2&3 pyramidal cells show positive phase in their mean phase shift profile which represents a lag in L2&3 pyramidal cells

bioRxiv preprint doi: https://doi.org/10.1101/748988; this version posted April 17, 2021. The copyright holder for this preprint (which was not certified by peer review) is the author/funder, who has granted bioRxiv a license to display the preprint in perpetuity. It is made available under aCC-BY-NC-ND 4.0 International license.

compared to L5 pyramidal cells (p<0.05; Mann-Whitney U). **d** Mean spike triggered average (STAs) for L5 and L2&3 neurons. Difference in STAs indicate L5 neurons require less current and instantaneous rate of current increase to initiate a spike (greater excitability). **e,f** Frequency dependent gain profile (mean ± one standard deviation) of L2&3 (n=3; RMP: -66.2±2.9 mV, Input resistance: 105± 26.46 MΩ) (e) and L5 (n=3; RMP: -66.8±3.1 mV, Input resistance: 81.3± 12 MΩ) (f) pyramidal cells before and after I_h blocker (ZD7288 10 µM). ZD7288 abolished the low frequency peaks in L5 neurons with little change in frequency dependent gain in L2&3 neurons. Source data are provided as a Source Data file.

Considerable heterogeneity and overlap in electrophysiological features among pyramidal cells sampled across different layers of the human neocortex

Given the large degree of variability among intrinsic electrophysiological features in the pyramidal cells in our study, we next sought to identify gradients or sub-clusters among these neurons. For example, in rodent neocortex, there is strong convergent evidence that pyramidal cells from L5 are split into two major subclasses, with neurons from L5a more likely to be regular spiking, IT projecting. IT cells show slender tufted dendritic morphologies compared to pyramidal cells in L5b, which are more likely to be bursting, ET, and show thick-tufted dendritic morphologies [29,41]. In the human neocortex there is evidence for this dichotomy based on transcriptomics data, although there are likely far fewer ET neurons than IT neurons in human L5 relative to the rodent (Supplementary Fig. 9) [26], which to our knowledge has yet to be corroborated at the electrophysiological and morphological levels.

We addressed this question using dimensionality reduction techniques to arrange our neurons by similarity in multi-variate sets of electrophysiological features (L2&3: n=56, L3c: n=14, L5: n=103 neurons). We specifically used UMAP [42] using 14 subthreshold and suprathreshold electrophysiological features that were consistently calculated in the majority of pyramidal cells within our dataset (see Methods). We found some evidence for gradients and/or subclusters among the sampled neurons based on the input electrophysiological features (Fig. 6a). Upon further inspection we found that a single major factor related to cell input resistance and rheobase current appeared to qualitatively define the major gradient underlying the differences in neurons highlighted by this analysis (Fig. 6b). We were able to corroborate aspects of this unbiased analysis through inspection of pyramidal cell morphologies (where available) with neurons at one extreme of the gradient having the largest input resistances and the most simple morphologies (e.g., cell a and cell f from Figure 1). Similarly, neurons with morphologies on the other side of the gradient tended to have lower input resistances and more complex morphologies such as the larger cell (cell g) shown in Figure 1. This analysis also revealed that neurons throughout the gradient tend to show bursting behavior (Fig. 6c) and that neurons with intermediate input resistances (such as those sampled from L3c) are more likely to display subthreshold resonance (Fig. 6d).

The other major finding of this analysis is that neurons from each of the layers we sampled were often inter-mixed in the low-dimensional space, with neurons from L2&3 often displaying very similar electrophysiological profiles to those sampled in L5. The pyramidal cells sampled from L3c were one exception, as these were present primarily at a single position in the low-dimensional space along with other neurons of intermediate input resistance. As we did not see strong evidence for a subtype of L5 neurons that were electrophysiologically distinct from those in L2&3 and other L5 neurons, we conclude that either we do not have L5 ET neurons present in our dataset (a strong possibility given their rarity, shown in Supplementary Fig. 9 [26]) or that we are unable to distinguish them from IT neurons using electrophysiological features alone (see Discussion). In summary, these findings are largely consistent with recent transcriptomics data [26] that strongly suggests that layer membership is not particularly informative

bioRxiv preprint doi: https://doi.org/10.1101/748988; this version posted April 17, 2021. The copyright holder for this preprint (which was not certified by peer review) is the author/funder, who has granted bioRxiv a license to display the preprint in perpetuity. It is made available under aCC-BY-NC-ND 4.0 International license.

dimension regarding pyramidal cell type diversity in human cortex, as many discrete transcriptomically defined cell types do not obey strict laminar boundaries.

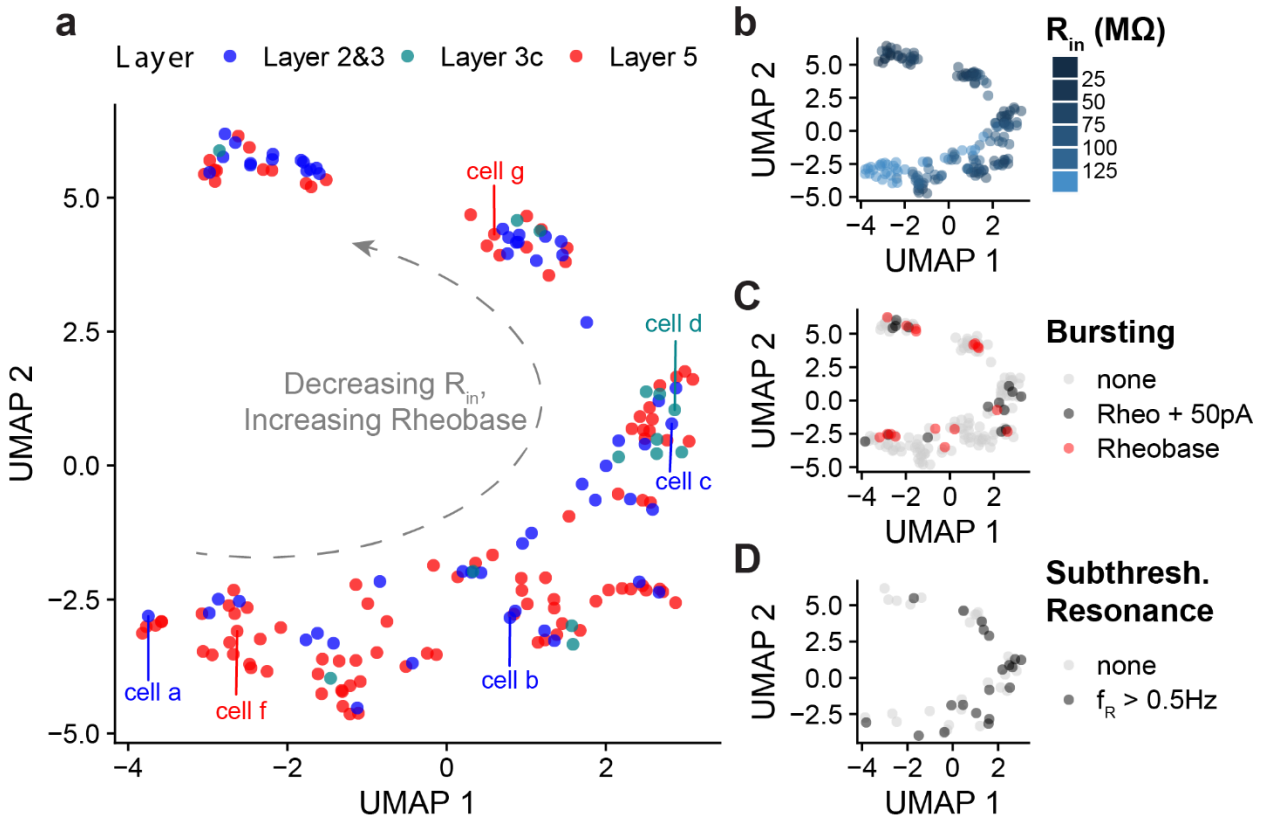

Figure 6. Dimensionality reduction reveals considerable intrinsic electrophysiological similarity and overlap between pyramidal cells recorded in different layers. a Dimensionality reduction analysis performed on multivariate sets of electrophysiological features using Uniform Manifold Approximation (UMAP). Neurons are arranged by similarity in intrinsic electrophysiological features (see methods for list of features used in analysis). Cell counts: L2&3: n=56, L3c: n=14, L5: n=103 neurons. Cell labels correspond to neurons whose morphologies are highlighted in **Figure 1**. **b, c, d** Same as **a**, but neurons are colored by input resistance (b), bursting behavior (c), or subthreshold resonance (d). Bursting behavior in **c** is broken down by neurons that show no bursting, neurons that burst at rheobase current plus 50 pA, or neurons that burst at rheobase. Bursting is defined where the instantaneous firing rate is greater than 75Hz. Source data are provided as a Source Data file.

Putative interneurons recorded in L5 show greater amounts of sag and subthreshold resonance relative to L2&3

Our data set also included several putative GABAergic interneurons (examples in Supplementary Fig. 7a; L2&3: n=10, L5: n=14). We were able to distinguish putative interneurons from pyramidal cells by their action potential characteristics (Supplementary Fig. 7b, c), large maximal firing rates, and typically large spike after-hyperpolarization amplitudes (see Supplementary Fig. 8 for morphological corroboration for one putative interneuron from our dataset). We found the set of putative interneurons in L5 had larger sag voltage amplitudes compared to putative interneurons in L2&3 (L2&3: 1.2 ± 1.1 mV, L5: 4.5± 3.7 mV,

bioRxiv preprint doi: https://doi.org/10.1101/748988; this version posted April 17, 2021. The copyright holder for this preprint (which was not certified by peer review) is the author/funder, who has granted bioRxiv a license to display the preprint in perpetuity. It is made available under aCC-BY-NC-ND 4.0 International license.

p=0.001; Supplementary Fig. 7d). Moreover, L5 putative interneurons had significantly larger rebound depolarization amplitudes relative to L2&3 putative interneurons (L2&3: 1.7 ± 2.2 mV, L5: 5.2± 3.2 mV, p=0.003; Supplementary Fig. 7e). Moreover, while there was a relatively small number of interneurons that were characterized with ZAP current injection (examples in Supplementary Fig. 7f, g), we noticed a comparatively large fraction of L5 putative interneurons that displayed a non-zero peak in their resonant frequency (3 of 6 neurons) compared to L2&3 (1 of 3 neurons) (Supplementary Fig. 7h). Although a small number of neurons and thus requiring corroboration, these data are consistent with prior reports of strong subthreshold resonance activity in human cortical GABAergic interneurons [5] and in rodent hippocampal interneurons [43].

Discussion

Guided by our previous work implicating deep layer human pyramidal cells in driving coherent low frequency oscillations in human neocortex, we sought to characterize how the electrophysiological differences between deep and superficial human pyramidal cells might inform the distinct role deep layer cells might play in cortical oscillations. We summarize four major findings from this work.

First, considering each broad cortical layer as a group, we found that there is a gradient of increased excitability from superficial to deeper layer pyramidal cells, with L2&3 pyramidal cells demonstrating more hyperpolarized resting potentials, lower input resistances and larger rheobase required for spike generation, enhanced spike frequency adaptation, and steeper and larger amplitude spike triggered averages. Along most of these features, the neurons sampled from L3c were often at an intermediate point between L2&3 and L5.

Second, we found enhanced sag and I_h-related features in L5 neurons relative to L2&3 neurons, again with L3c neurons intermediate between these groups. I_h appeared to be one of the major contributors to the prominent rebound depolarization and rebound spiking in human L5 neurons, as ZD7288 significantly reduced both. I_h also contributed to enhanced frequency-dependent gain at delta in L5 relative to L2&3 pyramidal cells being abolished using the I_h blocker ZD7288. Voltage-clamp data suggested this prominence of I_h in L5 pyramidal cells was due to increased channel number and not differences in kinetics of I_h channels. Intriguingly, we found anecdotal evidence that I_h appears more prominent in L5 relative to L2&3 putative GABAergic interneurons, and that this might contribute to enhanced resonant activity in these neurons.

Third, while we identified numerous pyramidal cells displaying non-zero resonant peaks in each cortical layer, we found resonance at frequencies >2Hz to be a largely uncommon feature. This corresponds with previous reports finding cells, albeit rarely, exhibiting resonance at >4Hz in the deeper parts of L3[4] and in larger, thick-tufted neurons in L5[3]

Fourth, we found a great degree of electrophysiological heterogeneity among pyramidal cells sampled within each cortical layer. Consistent with recent reports describing the variability in morpho-electric and transcriptomic subtypes of L2 and L3 pyramidal cells [4,27,28], we found a similar and potentially greater amount of electrophysiological variability among human L5 pyramidal cells. Such biophysical variability amongst neurons of the same cell-type is an increasingly recognized and computationally important aspect of neural circuits [44-46]. Our sampling of L5 pyramidal neurons is consistent with recent transcriptomic evidence suggesting that the vast majority of excitatory neurons in human L5 MTG are IT projecting [26]. Another source of variability arises from the known dichotomy between L5 ET and IT projecting neurons, which have been extensively characterized in rodents [29,41]. This source of variance is less likely a contributor

bioRxiv preprint doi: https://doi.org/10.1101/748988; this version posted April 17, 2021. The copyright holder for this preprint (which was not certified by peer review) is the author/funder, who has granted bioRxiv a license to display the preprint in perpetuity. It is made available under aCC-BY-NC-ND 4.0 International license.

to the biophysical variability we observe since IT cells make up only 0.6% of glutamatergic neurons in human L5 (Supplementary Fig.9). Thus, unlike a recent report [3] that targeted L5 thick-tufted neurons, the majority of the L5 neurons sampled here with their relatively high input resistances (>90 MΩ) suggests we recorded primarily from the abundant thin-tufted IT pyramidal cells. We note that disentangling these hypotheses requires further corroboration, and will likely require the use of emerging tools such as Patch-seq [27] to merge cell taxonomies along multiple modalities.

Given our findings of greater I_h in L5 neurons, we were initially surprised that a larger number of neurons did not demonstrate a peak in subthreshold resonance at frequencies >4Hz. For example, a previous report by Kalmbach et al. suggested that I_h contributes to prominent subthreshold resonance in deep L3 human pyramidal cells [4]. Similarly, somatic subthreshold resonance has also been reported in human L5 thick-tufted neurons [3]. In addition, previous work in rodents has shown that L5 pyramidal cells are endowed with subthreshold resonance [47-50]. However, our findings are not inconsistent with previous results in the human setting. In particular, the work of Kalmbach et al. reports notably few cells in L2&3 exhibiting subthreshold resonance at >4Hz, as well as many cells exhibiting no resonant peak at all when held at a common membrane potential of -65mV [4]. Similarly, we note that while Beaulieu-Laroche et al. reported strong subthreshold resonance among L5 pyramidal cells, these recordings were intentionally targeted towards the largest cells in L5 (and are thus likely to reflect characterization of the rare ET cells [3,26]).

It is worth emphasizing that subthreshold resonance is a complex dynamic not dictated solely by the amount of I_h present in a cell, which likely explains the minor differences in proportions of resonant cells reported in our work and that of Kalmbach et al. [4]. In fact, interactions between I_h [48], persistent Na^+ current (I_{NaP}), K_{IR} (instantaneously activating, inwardly rectifying K^+ current) [49], M-current [21] and passive properties [50] are all thought to influence this dynamic. Hippocampal oriens-lacunosum molecular (OLM) interneurons [43], CA1 pyramidal cells, oriens-radiatum (OR) interneurons [43], and inferior olivary neurons [51] are all examples of cells where subthreshold resonance is not solely and/or directly driven by I_h. When viewed in concert with our recent detailed computational investigation of the relationship between I_h and subthreshold resonance [31], our current results serve to highlight that a prominent I_h is not always sufficient to drive subthreshold resonance. With subthreshold resonance not observed as a general feature of L5 pyramidal cells, we sought other biophysical features that might explain why L5 cells appear to drive interlaminar theta coherence. Recently, a putative "dynamic circuit motif" (DCM) [20] has been proposed to underlie the interlaminar nested delta-theta oscillations observed in rodents. This DCM posits intrinsically-bursting (IB) neurons in L5 neurons as central actors in generating deep layer activity that drives superficial theta oscillations [52]. Although the electrophysiological signature and experimental conditions studied in Carracedo et. al. were different to ours in human cortical slices [9], it is instructive to relate our findings to what was observed in rat neocortex. Carracedo et. al. demonstrated that delta oscillations likely occur due to tonic drive to the dendrites of IB neurons in superficial layers [52]. This tonic drive causes the IB neurons to discharge bursts at delta frequencies (~2Hz). IB neurons are unique in that, in addition to their subcortical targets, they primarily synapse locally within deep layers on L5 RS IT neurons, unlike L5 RS neurons that project axons both locally and to L2&3 [41,53,54]. The RS neurons are thus driven by periodic barrages at delta frequencies and discharge doublets with each IB burst, thus generating "theta" frequency output at double the L5 delta frequency, which is then transmitted to superficial layers. The sinks generated in the superficial layers thus occur at theta frequency, driving local excitability in L2&3 with the resultant increase in excitatory drive to L5 IB dendrites starting the cycle anew.

Our results demonstrating 4 and 8Hz peaks in *G(f)* for L5 RS neurons, interpreted in the context of the above findings by Carracedo et al., provides a plausible mechanism for the theta activity (~8Hz) we observed in vitro [55] and which is ubiquitously observed in the human brain [17]. It is important to note that

bioRxiv preprint doi: https://doi.org/10.1101/748988; this version posted April 17, 2021. The copyright holder for this preprint (which was not certified by peer review) is the author/funder, who has granted bioRxiv a license to display the preprint in perpetuity. It is made available under aCC-BY-NC-ND 4.0 International license.

the theta generated by RS neurons described by Carracedo et al. arises from the doublet generated in response to each cycle of delta, and thus why theta (~4Hz) was twice the frequency of the observed delta (~2Hz) in their work. The double peak in *G(f)* we observe in human L5 RS neurons implies that RS neurons are tuned to both 4Hz and 8Hz activity, and not surprisingly the 8Hz peak in *G(f)* is similar to the frequency at which interlaminar coherence was observed in human slices [9], and twice the frequency of the low frequency peak in *G(f)*. Our ZD data further supports this relationship between the delta and theta peaks, where the delta peak in *G(f)* in a different subset of neurons was ~5.5Hz, and the "theta" peak was at ~11Hz. That blocking I_h abolished the delta peak suggests that I_h tunes L5 RS neurons to track IB output, which in turn generates theta (double the frequency of delta) output. Interpreted together, our frequency dependent gain and ZAP results suggest that I_h may not be a direct "cause" of cortical oscillations at theta (~8Hz), but rather tune RS cells to follow with great fidelity the IB output at delta (see Supplementary Fig. 10 for this dynamic circuit motif).

An obvious difference between our previous human slice work [9] and that of Carracedo et al. is that we observed robust deep layer theta, although theta was still more prominent in the superficial layers. One possible explanation is that it has been shown that in human L2&3, a single action potential generates long lasting reverberant activity through rebound excitation that lasts an order of magnitude longer than in the rodent [7]. Thus, it is possible that such reverberant activity as well exists in L5 resulting in greater gain in local L5 cortical circuits that amplifies theta activity through both synaptic activation, and the theta peak in *G(f)*. This conjecture is further supported by our observation that putative L5 interneurons demonstrate greater rebound depolarization than L2&3 neurons, and thus are likely able to amplify network activity within L5 potentially beyond what was observed in L2&3 [7]. Future experiments are needed to explore if human cortical circuitry is arranged like that of the rodent, specifically as it relates to inter- and intralaminar connectivity.

It bears acknowledging that experimental limitations might have influenced our observation of subthreshold resonance. The increased density of the HCN channel in dendrites may result in resonance being observed better in the dendrites compared to the soma [3], and despite best practice controls the possibility remains that truncated dendrites might affect resonance. Truncation of layer 5 pyramidal cell dendrites is a common and unavoidable issue due to longer apical dendrite length in the human neocortex (2mm) [1,3]. However, there is strong evidence for increased dendritic compartmentalization in large human neurons with distal inputs attenuating strongly towards soma [3], and one would expect this effect to mitigate any effects of dendritic truncation on subthreshold resonance.

An important caveat when interpreting these findings is that these data are exclusively collected from neurosurgical patients undergoing surgery for drug-resistant epilepsy or for resection of brain tumors. We have been careful to only record from unaffected (non-epileptogenic) neocortical tissue. Nevertheless, it is unclear how these diseases (or their pharmacological treatment regimes) might contribute to compensatory changes at the level of cortical neuron physiology. Notwithstanding that epilepsy patients represent the primary source of viable human tissue for in vitro human studies [1,3,4,26], our data is comparable to these human cell-typing efforts, since our inclusion criteria for our samples is consistent with these human studies**.** Additionally, by comparing our findings to analogous human neuronal datasets collected by other groups, we are confident our results are comparable to similar human cell-type characterizations. Lastly the most ubiquitous source of tissue from this study (MTG of epilepsy patients) demonstrates seeming transcriptomic "normalcy" when compared to post-mortem specimens from the MTG [26].

This report reflects one of the largest studies of the electrophysiological diversity of human neocortical pyramidal cells to date, contributing to our growing understanding of human L5 pyramidal cells [3] and

bioRxiv preprint doi: https://doi.org/10.1101/748988; this version posted April 17, 2021. The copyright holder for this preprint (which was not certified by peer review) is the author/funder, who has granted bioRxiv a license to display the preprint in perpetuity. It is made available under aCC-BY-NC-ND 4.0 International license.

serving to put the unique characteristics of these neurons into context with the better understood superficial layer pyramidal cells. Specifically, our unbiased sampling strategy of L5 cells complements the targeted characterization of large, thick-tufted L5 human pyramidal cells recently reported [3]. Given the rare opportunity to perform experiments in live human tissue, our work also represents an extremely valuable opportunity to compare findings with the limited existing literature on electrophysiological properties of human cortical neurons.

Moving forward, it will be essential to reconcile these electrophysiological and morphological data with the emerging consensus of neocortical cell type diversity based on single-cell transcriptomics [3,4,26,56] and how these features contribute to the unique emergent properties of human cortical circuits. Furthermore, little is known about the connectivity within human cortical circuits: is human inter- and intra-laminar connectivity similar to rodents, and how do cellular properties contribute to the signatures observed in meso- and macroscopic recordings? Answering these questions will require multi-scale inquires of human cortical micro-circuits and *in silico* experiments to understand the divergent properties of human circuits, with the tools for such inquiries only now becoming available.

Methods

Human brain slice preparation

Written informed consent was obtained from all study participants to use their tissue as well as to share the acquired electrophysiological data and anonymized demographic information – including age, sex, years of seizure, diagnosis, and antiepileptic drug treatment – as stated in the research protocol. In accordance with the Declaration of Helsinki, approval for this study was received by the University Health Network Research Ethics board. Sixty-one patients, age ranging between 19 to 63 years (Mean age: 37.1 ± 1.8), underwent a standard anterior temporal lobectomy (ATL) [57] or tumor resection from the frontal or temporal lobe [58,59] under general anesthesia using volatile anesthetics.

The surgery involved resecting the first 4.5 cm of neocortex using sharp dissection and local cooling with ~4°C TissueSol®. Immediately following surgical resection, the cortical block was submerged in an ice-cold (~4°C) cutting solution that was continuously bubbled with 95% O_2-5% CO_2 containing (in mM) sucrose 248, KCl 2, $MgSO_4.7H_2O$ 3, $CaCl_2.2H_2O$ 1, $NaHCO_3$ 26, $NaH_2PO_4.H_2O$ 1.25, D-glucose 10. The osmolarity was adjusted to 300-305 mOsm. The total duration, including slicing and transportation, was kept to a maximum of 20 minutes [59]. Transverse brain slices (400 µm) were obtained using a vibratome (Leica 1200 V) in cutting solution. Tissue slicing was performed perpendicular to the pial surface to ensure that pyramidal cell dendrites were minimally truncated [4,58]. The cutting solution was the same as used for transport of tissue from operation room to the laboratory. After sectioning, the slices were incubated for 30 min at 34°C in standard artificial cerebrospinal fluid (aCSF) (in mM): NaCl 123, KCl 4, $CaCl_2.2H_2O$ 1, $MgSO_4.7H_2O$ 1, $NaHCO_3$ 26, $NaH_2PO_4.H_2O$ 1.2, and D-glucose 10, pH 7.40. All aCSF and cutting solutions were continuously bubbled with carbogen gas (95% O_2-5% CO_2) and had an osmolarity of 300-305 mOsm. Following this incubation, the slices were maintained in standard aCSF at 22–23 °C for at least 1 hour, until they were individually transferred to a submerged recording chamber.

For a subset of experiments designed to assess frequency dependent gain, slices were prepared using the NMDG protective recovery method [60]. The slicing and transport solution was composed of (in mM): NMDG 92, KCl 2.5, NaH_2PO_4 1.25, $NaHCO_3$ 30, HEPES 20, Glucose 25, Thiourea 2, Na L-ascorbate 5, Na-Pyruvate 3, $CaCl_2.4H_2O$ 0.5, and $MgSO_4.7H_2O$ 10. The pH of NMDG solution was adjusted to 7.3-7.4 using hydrochloric acid and the osmolarity was 300-305 mOsm. Before transport and slicing, the NMDG solution was carbogenated for 15 min and chilled to 2-4°C. After slices were cut (as described above), they were transferred to a recovery chamber filled with 32-34°C NMDG solution, and continuously bubbled with 95%

bioRxiv preprint doi: https://doi.org/10.1101/748988; this version posted April 17, 2021. The copyright holder for this preprint (which was not certified by peer review) is the author/funder, who has granted bioRxiv a license to display the preprint in perpetuity. It is made available under aCC-BY-NC-ND 4.0 International license.

O_2 5% CO_2. After 12 minutes, the slices were transferred to an incubation solution containing (in mM): NaCl 92, KCl 2.5, $NaH_2PO_4.H_2O$ 1.25, $NaHCO_3$ 30, HEPES 20, Glucose 25, Thiourea 2, Na L-ascorbate 5, Na-Pyruvate 3, $CaCl_2.4H_2O$ 2, and $MgSO_4.7H_2O$ 2. The solution was continuously bubbled with 95% O_2 -5% CO_2. After 1 hour incubation at room temperature, slices were transferred to a recording chamber and continuously perfused with aCSF containing (in mM): NaCl 126, KCl 2.5, $NaH_2PO_4.H_2O$ 1.25, $NaHCO_3$ 26, Glucose 12.6, $CaCl2.2H_2O$ 2, and $MgSO_4.7H_20$ 1. We emphasize that these experiments were performed with excitatory (APV 50 µM, Sigma; CNQX 25 µM, Sigma) and inhibitory (Bicuculline 10 µM, Sigma; CGP-35348 10 µM, Sigma) synaptic activity blocked. These blockers are only used in these experiments, highlighted in Figure 5.

Electrophysiology recordings and intrinsic physiology feature analysis

For recordings, slices were transferred to a recording chamber mounted on a fixed-stage upright microscope (Olympus BX_{51}WI upright microscope; Olympus Optical Co., NY, USA and Axioskop 2 FS MOT; Carl Zeiss, Germany). Slices were continually perfused at 4 ml/min with standard aCSF at 32-34°C. Cortical neurons were visualized using an IR-CCD camera (IR-1000, MTI, USA) with a 40x water immersion objective lens. Using the IR-DIC microscope, the boundary between layer 1 and 2 was easily distinguishable in terms of cell density. Below L2, the sparser area of neurons (L3) were followed by a tight band of densely packed layer 4 (L4) neurons. L4 was followed by a decrease in cell density (L5). In general, we did not annotate different neurons recorded from L2 versus those recorded from L3, except when explicitly mentioned. In this study, we use the terminology "L2&3" to highlight that these layers are distinct in the human cortex, rather than indistinguishable as in the rodent cortex. Cells specifically targeted in deep L3 are further distinguished by being denoted as coming from "L3c".

Patch pipettes (3-6 MΩ resistance) were pulled from standard borosilicate glass pipettes (thin-wall borosilicate tubes with filaments, World Precision Instruments, Sarasota, FL, USA) using a vertical puller (PC-10, Narishige). Pipettes were filled with intracellular solution containing (in mM): K-gluconate 135; NaCl 10; HEPES 10; $MgCl_2$ 1; Na_2ATP 2; GTP 0.3, pH adjusted with KOH to 7.4 (290–309 mOsm). In a subset of experiments the pipette solution also contained biocytin (3-5%). Whole-cell patch-clamp recordings were obtained using a Multiclamp 700A amplifier, Axopatch 200B amplifier, pClamp 9.2 and pClamp 10.6 data acquisition software (Axon instruments, Molecular Devices, USA). Subsequently, electrical signals were digitized at 20 kHz using a 1320X digitizer. The access resistance was monitored throughout the recording (typically between 8-25 MΩ), and neurons were discarded if the access resistance was >25 MΩ. The liquid junction potential was calculated to be -10.8 mV and was not corrected.

Data were analysed off-line using Clampfit 10.7, Python, MATLAB, and R software. The resting membrane potential (RMP) was measured after breaking into the cell (IC=0). The majority of the intrinsic electrophysiological features reported here were calculated using the Python IPFX toolbox (https://github.com/AllenInstitute/ipfx/) with default parameter settings [61]. The input resistance and membrane time constant were calculated using hyperpolarizing sweeps between -50 to -200pA. Single action potential features, the like action potential threshold, peak, width at half-max, and the upstroke-downstroke ratio, were calculated using the first spike at rheobase. The adaptation index, average firing rate, inter-spike intervals (first, mean, median, coefficient of variation) were defined using the "hero" sweep with default parameters (defined as the sweep between 39 to 61 pA greater than the rheobase). Sag amplitude and sag ratio were defined in response to hyperpolarizing current pulses (600ms duration, 0 to -400 pA, 50 pA steps). The sag ratio was calculated as the difference between the minimum value and the steady state divided by peak deflection during hyperpolarization current injection. The rebound depolarization amplitude was calculated as the difference between the steady state voltage and the maximum depolarization potential. We also observed the presence or absence of rebound spiking following

bioRxiv preprint doi: https://doi.org/10.1101/748988; this version posted April 17, 2021. The copyright holder for this preprint (which was not certified by peer review) is the author/funder, who has granted bioRxiv a license to display the preprint in perpetuity. It is made available under aCC-BY-NC-ND 4.0 International license.

the injection of hyperpolarization current steps (-400 pA). The I_h blocker ZD7288 (10 μM, Sigma Aldrich) was applied to confirm pharmacological evidence for I_h.

Bursting neurons were defined as those where the instantaneous frequency (determined by the first inter-spike interval at rheobase) was greater than 75Hz. We identified putative interneurons within our dataset by manually assessing each cell's maximum firing rates, spike widths, and after-hyperpolarization amplitudes. Putative interneurons that we identified using these criteria typically had spike half-widths less than <1 ms, afterhyperpolarization amplitudes greater than 10mV, and maximum firing rates >75Hz [62]. We note that one limitation of this intrinsic feature-based identification criteria is the relative inability to identify VIP and other CGE (Caudal Ganglionic Eminence) -derived interneurons using intrinsic electrophysiological criteria alone[63] .

Voltage-clamp characterisation of I_h and I_{tail}

To characterize I_h, 600 ms-long voltage-clamp steps were used in -10mV increments, down to -140mV from a holding potential of -60mV. In order to measure I_h amplitude, the difference between the steady state at the end of the holding potential and the maximum current was determined. The I_{tail} was quantified as the difference between peak amplitude of residual current at the end of each holding potential and the steady state current from holding potentials of -140 to -60mV. A single or double-exponential model, fitted to the various currents recorded, was used to calculate the time constants of I_h in order to determine the kinetics of I_h. To measure the voltage sensitivity of I_h in L2&3 and L5 pyramidal cells, the membrane potential evoking half-maximal activation of I_h (V_{50}) was obtained by fitting the I_h activation to a Boltzmann sigmoid function using GraphPad 6 (GraphPad, San Diego, CA, USA). In experiments to quantify I_h, the sodium channel blocker tetrodotoxin (1 μM; Alomone Labs) to block voltage gated sodium currents, $CoCl_2$ (2mM; Sigma-Aldrich) to block voltage-sensitive calcium currents, and $BaCl_2$ (1mM; Sigma-Aldrich) to block inwardly rectifying potassium current were added to the bath solution. We note that space clamp issues limit the precise quantification of the I_h [30].

Subthreshold resonance and spike probability analyses

To assess subthreshold and suprathreshold resonance properties, a frequency modulated sine wave current input (ZAP/chirp) was generated ranging from 1 to 20Hz, lasting 20 seconds [33] with a sampling rate of 10kHz. This current waveform was then injected using the custom waveform feature of Clampex 9.2 and Clampex 10.2 (Axon Instruments, Molecular Devices, USA). The subthreshold current amplitude was adjusted to the maximal current that did not elicit spiking.

For determining subthreshold resonance, only trials without spiking were utilized for analysis. Analyses were performed using in house Python scripts adapted from Kalmbach et al. [4]. The impedance profile of the cell was computed by taking the ratio of the voltage over current in the frequency domain obtained with the fast Fourier transform. Window averaging was then applied to smooth the impedance profile of the cell. The impedance profiles were then averaged over several trials (up to five) to obtain the mean impedance profile of the cell. The frequency point with the highest impedance is the center frequency while the frequency point with half of the center impedance is the 3dB cut-off frequency. Resonant neurons were defined as those with resonant frequencies greater than 0.5Hz, the lowest frequency tested here.

To analyze responses to suprathreshold frequency-modulated sinusoidal current, spiking probability as a function of input frequency was assessed using suprathreshold current stimulation. The suprathreshold current was set by gradually increasing the amplitude of the ZAP function input by adjusting the gain of the stimulus until the first spike was elicited. Ten traces per cell were utilized to obtain the probability of spiking as a function of frequency. Since the instantaneous frequency is known from the current input, each action potential could be assigned a frequency at which it occurred. To create the spike probability density

bioRxiv preprint doi: https://doi.org/10.1101/748988; this version posted April 17, 2021. The copyright holder for this preprint (which was not certified by peer review) is the author/funder, who has granted bioRxiv a license to display the preprint in perpetuity. It is made available under aCC-BY-NC-ND 4.0 International license.

function for each cell type, the frequencies at which individual spikes occurred were pooled, a histogram generated and divided by the total number of spikes. To compare spike probability density functions between cell types the distributions were compared using a two-sample Kolmogorov-Smirnov test (`kstest2.m`).

Multi-variate electrophysiological feature analysis

We used a dimensionality reduction approach to visualize similarities in recorded neurons according to multi-variate correlations in measured electrophysiology features. We specifically used the uniform manifold approximation (UMAP) function and library implemented in R with default parameter settings [42]. We defined each recorded cell using feature vectors constructed from a set of 14 electrophysiological features that were reliably calculated in most characterized neurons. We specifically used the following subthreshold features: resting membrane potential, input resistance, membrane time constant, sag ratio, sag amplitude. We additionally used the following suprathreshold features of the first action potential at rheobase: AP threshold, amplitude, half-width, upstroke-downstroke ratio, after-hyperpolarization amplitude, rheobase, and latency to first spike. We also used the following spike train features: slope of FI curve and average spiking rate at the hero sweep stimulus.

Frequency Dependent Gain

Following a similar methodology of Higgs et al. [38], frequency dependent gain was computed using 30 trials (inter-trial interval = 20 seconds) of a 2.5 second duration current injection stimulus of frozen white noise convolved with a 3ms square function [64]. This measure identifies the likelihood of the neuron spiking in phase with an oscillatory input that is small relative to the overall input to the cell, distinct from analysis of the neuron's activity in response to a suprathreshold ZAP input [38]. The amplitude (a.k.a. variance) of the current injection stimulus was scaled to elicit spike rates of above 5Hz, the typical firing rate for cortical pyramidal cells [65]. In addition to increasing the noise variance, a steady amount of DC current was required [38] to elicit spiking, which was delivered as various amplitude steps were added to the noisy current input. Peaks detected in the voltage time series with overshoot greater than 0mV were taken to be the occurrence of an action potential. The time varying firing rate *r(t)* was given by:

$$r(t) = \begin{cases} \frac{1}{\Delta t} & \text{Where spike detected} \\ 0 & \text{Where no spike detected} \end{cases} \quad (1)$$

The stimulus–response correlation (c_{sr}) and the stimulus autocorrelation (c_{ss}) were calculated in the following fashion:

$$c_{sr}(\tau) = \langle s(t) r(t+\tau) \rangle \quad (2)$$

$$C_{ss}(\tau) = \langle s(t) s(t+\tau) \rangle \quad (3)$$

where τ is the time difference, and the stimulus $s(t)$ is $I_{noise}(t)$. After windowing the $c_{sr}(\tau)$ and $c_{ss}(\tau)$ functions (see below), the complex Fourier components $C_{sr}(f)$ and $C_{ss}(f)$ were obtained, and the frequency-dependent gain and the average phase shift were calculated with $\sigma = 1/f$, in order to ensure the spectral estimates were not dominated by noise. The gain (G(f)) and the phase ($\varphi(f)$) are:

$$G(f) = \frac{|C_{sr}(f)|}{|C_{ss}(f)|} \quad (4)$$

$$\varphi(f) = atan \frac{[\mathrm{Im}[C_{sr}(f)]]}{[\mathrm{Re}[C_{sr}(f)]]} \quad (5)$$

bioRxiv preprint doi: https://doi.org/10.1101/748988; this version posted April 17, 2021. The copyright holder for this preprint (which was not certified by peer review) is the author/funder, who has granted bioRxiv a license to display the preprint in perpetuity. It is made available under aCC-BY-NC-ND 4.0 International license.

where Re and Im refer to the real and imaginary parts of each Fourier component. φ(f) was then corrected using the peak time (τ_{delay}) of $c_{sr}(\tau)$ [38].

For statistical testing, individual gains or *G(f)*s for each cell (30 trials/cell) from neurons with spike rates above 5Hz were pooled for each cell type. To compare between cell types, Mann-Whitney U (`ranksum.m`) was used to obtain a *p*-value at each frequency (2-100Hz in 0.2Hz steps). The *p*-values were the false discovery rate corrected with an alpha = 0.01 [40].

Histological methods

During electrophysiological recording, biocytin (3-5 mg/ml) was allowed to diffuse into the patched neuron; after 20-45 minutes, the electrodes were slowly retracted under visual guidance to maintain the quality of the seal and staining. The slices were left for another 10-15 minutes in the recording chamber to washout excess biocytin from extracellular space, then transferred to 4% paraformaldehyde and kept at 4°C for 24 hours.

Subsequently, the slices were washed and transferred into PBS solution (0.1 mM). To reveal biocytin, slices were incubated in blocking serum (0.5 % Bovine serum albumin (BSA), 0.5 % milk powder) and 0.1% Triton X-100 in PBS for 1 hour at room temperature. Finally, slices were incubated with streptavidin-conjugated Alexa Fluor 594 (1:300) overnight at 4°C. Then slices were rinsed with PBS and mounted on the slide using moviol (Sigma-Aldrich). Imaging was done using a Zeiss LSM710 Multiphoton microscope. Reconstructions were performed using IMARIS software (Bitplane, Oxford instrument company).

Statistical analyses

Statistical analyses and plotting were performed using GraphPad Prism 6. Data are presented in the text as mean ± SD unless otherwise noted. Unless stated otherwise, a standard threshold of $p<0.05$ was used to report statistically significant differences. One-Way ANOVA post hoc with Dunn's multiple comparison test were used for statistical comparison. The non-parametric Mann-Whitney test was used to determine statistical differences between two groups. Wilcoxon matched-pairs signed rank test used for paired comparison between two groups.

Data Availability

Source data are provided with this paper in the Supplementary Materials.

Code Availability

Computational code for custom analyses are available at the following GitHub repositories: https://github.com/stripathy/valiante_ih (R) and https://github.com/stripathy/valiante_lab_abf_process (Python).

References

1 Mohan, H. *et al.* Dendritic and axonal architecture of individual pyramidal neurons across layers of adult human neocortex. *Cerebral Cortex* **25**, 4839-4853 (2015).

2 Eyal, G. *et al.* Unique membrane properties and enhanced signal processing in human neocortical neurons. *Elife* **5**, e16553 (2016).

bioRxiv preprint doi: https://doi.org/10.1101/748988; this version posted April 17, 2021. The copyright holder for this preprint (which was not certified by peer review) is the author/funder, who has granted bioRxiv a license to display the preprint in perpetuity. It is made available under aCC-BY-NC-ND 4.0 International license.

3 Beaulieu-Laroche, L. *et al.* Enhanced dendritic compartmentalization in human cortical neurons. *Cell* **175**, 643-651. e614 (2018).

4 Kalmbach, B. E. *et al.* h-Channels Contribute to Divergent Intrinsic Membrane Properties of Supragranular Pyramidal Neurons in Human versus Mouse Cerebral Cortex. *Neuron* **100**, 1194-1208. e1195 (2018).

5 Boldog, E. *et al.* Transcriptomic and morphophysiological evidence for a specialized human cortical GABAergic cell type. *Nature neuroscience* **21**, 1185-1195 (2018).

6 Deitcher, Y. *et al.* Comprehensive morpho-electrotonic analysis shows 2 distinct classes of L2 and L3 pyramidal neurons in human temporal cortex. *Cerebral Cortex* **27**, 5398-5414 (2017).

7 Molnár, G. *et al.* Complex events initiated by individual spikes in the human cerebral cortex. *PLoS biology* **6**, e222 (2008).

8 Verhoog, M. B. *et al.* Mechanisms underlying the rules for associative plasticity at adult human neocortical synapses. *Journal of Neuroscience* **33**, 17197-17208 (2013).

9 Florez, C. *et al.* In vitro recordings of human neocortical oscillations. *Cerebral cortex* **25**, 578-597 (2015).

10 Goriounova, N. A. *et al.* Large and fast human pyramidal neurons associate with intelligence. *Elife* **7**, e41714 (2018).

11 Skinner, F. K. Cellular-based modeling of oscillatory dynamics in brain networks. *Current opinion in neurobiology* **22**, 660-669 (2012).

12 Womelsdorf, T., Ardid, S., Everling, S. & Valiante, T. A. Burst firing synchronizes prefrontal and anterior cingulate cortex during attentional control. *Current Biology* **24**, 2613-2621 (2014).

13 Markram, H. *et al.* Reconstruction and simulation of neocortical microcircuitry. *Cell* **163**, 456-492 (2015).

14 Einevoll, G. T. *et al.* The Scientific Case for Brain Simulations. *Neuron* **102**, 735-744 (2019).

15 Ruzzo, E. K. & Geschwind, D. H. Schizophrenia genetics complements its mechanistic understanding. *Nature neuroscience* **19**, 523 (2016).

16 Vigo, D. V., Kestel, D., Pendakur, K., Thornicroft, G. & Atun, R. Disease burden and government spending on mental, neurological, and substance use disorders, and self-harm: cross-sectional, ecological study of health system response in the Americas. *The Lancet Public Health* **4**, e89-e96 (2019).

17 Groppe, D. M. *et al.* Dominant frequencies of resting human brain activity as measured by the electrocorticogram. *Neuroimage* **79**, 223-233 (2013).

18 McGinn, R. J. & Valiante, T. A. Phase–amplitude coupling and interlaminar synchrony are correlated in human neocortex. *Journal of Neuroscience* **34**, 15923-15930 (2014).

19 von Nicolai, C. *et al.* Corticostriatal coordination through coherent phase-amplitude coupling. *Journal of Neuroscience* **34**, 5938-5948 (2014).

20 Womelsdorf, T., Valiante, T. A., Sahin, N. T., Miller, K. J. & Tiesinga, P. Dynamic circuit motifs underlying rhythmic gain control, gating and integration. *Nature neuroscience* **17**, 1031 (2014).

21 Hu, H., Vervaeke, K. & Storm, J. F. Two forms of electrical resonance at theta frequencies, generated by M-current, h-current and persistent Na+ current in rat hippocampal pyramidal cells. *The Journal of physiology* **545**, 783-805 (2002).

22 Das, A. & Narayanan, R. Theta-frequency selectivity in the somatic spike-triggered average of rat hippocampal pyramidal neurons is dependent on HCN channels. *Journal of neurophysiology* **118**, 2251-2266 (2017).

23 Neuhoff, H., Neu, A., Liss, B. & Roeper, J. Ih channels contribute to the different functional properties of identified dopaminergic subpopulations in the midbrain. *Journal of Neuroscience* **22**, 1290-1302 (2002).

bioRxiv preprint doi: https://doi.org/10.1101/748988; this version posted April 17, 2021. The copyright holder for this preprint (which was not certified by peer review) is the author/funder, who has granted bioRxiv a license to display the preprint in perpetuity. It is made available under aCC-BY-NC-ND 4.0 International license.

24 Gastrein, P. *et al.* The role of hyperpolarization-activated cationic current in spike-time precision and intrinsic resonance in cortical neurons in vitro. *The Journal of physiology* **589**, 3753-3773 (2011).

25 Herrmann, S., Schnorr, S. & Ludwig, A. HCN channels—Modulators of cardiac and neuronal excitability. *International journal of molecular sciences* **16**, 1429-1447 (2015).

26 Hodge, R. D. *et al.* Conserved cell types with divergent features in human versus mouse cortex. *Nature* **573**, 61-68 (2019).

27 Berg, J. *et al.* Human cortical expansion involves diversification and specialization of supragranular intratelencephalic-projecting neurons. *BioRxiv* (2020).

28 Ting, J. T. *et al.* A robust ex vivo experimental platform for molecular-genetic dissection of adult human neocortical cell types and circuits. *Scientific reports* **8**, 1-13 (2018).

29 Ramaswamy, S. & Markram, H. Anatomy and physiology of the thick-tufted layer 5 pyramidal neuron. *Frontiers in cellular neuroscience* **9**, 233 (2015).

30 Bar-Yehuda, D. & Korngreen, A. Space-clamp problems when voltage clamping neurons expressing voltage-gated conductances. *Journal of neurophysiology* **99**, 1127-1136 (2008).

31 Rich, S., Moradi Chameh, H., Sekulic, V., Valiante, T. A. & Skinner, F. K. Modeling Reveals Human–Rodent Differences in H-Current Kinetics Influencing Resonance in Cortical Layer 5 Neurons. *Cerebral Cortex*, doi:10.1093/cercor/bhaa261 (2020).

32 Hutcheon, B. & Yarom, Y. Resonance, oscillation and the intrinsic frequency preferences of neurons. *Trends in neurosciences* **23**, 216-222 (2000).

33 Hutcheon, B., Miura, R. M. & Puil, E. Subthreshold membrane resonance in neocortical neurons. *Journal of Neurophysiology* **76**, 683-697 (1996).

34 Richardson, M. J., Brunel, N. & Hakim, V. From subthreshold to firing-rate resonance. *Journal of neurophysiology* **89**, 2538-2554 (2003).

35 Rotstein, H. G. Frequency preference response to oscillatory inputs in two-dimensional neural models: a geometric approach to subthreshold amplitude and phase resonance. *The Journal of Mathematical Neuroscience* **4**, 11 (2014).

36 Rotstein, H. G. Spiking resonances in models with the same slow resonant and fast amplifying currents but different subthreshold dynamic properties. *Journal of computational neuroscience* **43**, 243-271 (2017).

37 Rotstein, H. G. & Nadim, F. Frequency preference in two-dimensional neural models: a linear analysis of the interaction between resonant and amplifying currents. *Journal of computational neuroscience* **37**, 9-28 (2014).

38 Higgs, M. H. & Spain, W. J. Conditional bursting enhances resonant firing in neocortical layer 2–3 pyramidal neurons. *Journal of Neuroscience* **29**, 1285-1299 (2009).

39 Yu, X. & Lewis, E. R. Studies with spike initiators: linearization by noise allows continuous signal modulation in neural networks. *IEEE Transactions on Biomedical Engineering* **36**, 36-43 (1989).

40 Benjamini, Y. & Hochberg, Y. Controlling the false discovery rate: a practical and powerful approach to multiple testing. *Journal of the royal statistical society. Series B (Methodological)*, 289-300 (1995).

41 Baker, A. *et al.* Specialized subpopulations of deep-layer pyramidal neurons in the neocortex: bridging cellular properties to functional consequences. *Journal of Neuroscience* **38**, 5441-5455 (2018).

42 McInnes, L., Healy, J., Saul, N. & Grossberger, L. UMAP: Uniform Manifold Approximation and Projection. *Journal of Open Source Software* **3**, 861, doi:10.21105/joss.00861 (2018).

43 Zemankovics, R., Káli, S., Paulsen, O., Freund, T. F. & Hájos, N. Differences in subthreshold resonance of hippocampal pyramidal cells and interneurons: the role of h-current and passive membrane characteristics. *The Journal of physiology* **588**, 2109-2132 (2010).

bioRxiv preprint doi: https://doi.org/10.1101/748988; this version posted April 17, 2021. The copyright holder for this preprint (which was not certified by peer review) is the author/funder, who has granted bioRxiv a license to display the preprint in perpetuity. It is made available under aCC-BY-NC-ND 4.0 International license.

44 Padmanabhan, K. & Urban, N. N. Intrinsic biophysical diversity decorrelates neuronal firing while increasing information content. *Nature neuroscience* **13**, 1276 (2010).

45 Tripathy, S. J., Padmanabhan, K., Gerkin, R. C. & Urban, N. N. Intermediate intrinsic diversity enhances neural population coding. *Proceedings of the National Academy of Sciences* **110**, 8248-8253 (2013).

46 Marder, E. Variability, compensation, and modulation in neurons and circuits. *Proceedings of the National Academy of Sciences* **108**, 15542-15548 (2011).

47 Silva, L. R., Amitai, Y. & Connors, B. W. Intrinsic oscillations of neocortex generated by layer 5 pyramidal neurons. *Science* **251**, 432 (1991).

48 Ulrich, D. Dendritic resonance in rat neocortical pyramidal cells. *Journal of neurophysiology* **87**, 2753-2759 (2002).

49 Dembrow, N. C., Chitwood, R. A. & Johnston, D. Projection-specific neuromodulation of medial prefrontal cortex neurons. *Journal of Neuroscience* **30**, 16922-16937 (2010).

50 Schmidt, S. L., Dorsett, C. R., Iyengar, A. K. & Fröhlich, F. Interaction of intrinsic and synaptic currents mediate network resonance driven by layer V pyramidal cells. *Cerebral Cortex* **27**, 4396-4410 (2016).

51 Lampl, I. & Yarom, Y. Subthreshold oscillations and resonant behavior: two manifestations of the same mechanism. *Neuroscience* **78**, 325-341 (1997).

52 Carracedo, L. M. *et al.* A neocortical delta rhythm facilitates reciprocal interlaminar interactions via nested theta rhythms. *Journal of Neuroscience* **33**, 10750-10761 (2013).

53 Chagnac-Amitai, Y., Luhmann, H. J. & Prince, D. A. Burst generating and regular spiking layer 5 pyramidal neurons of rat neocortex have different morphological features. *Journal of Comparative Neurology* **296**, 598-613 (1990).

54 Perin, R., Berger, T. K. & Markram, H. A synaptic organizing principle for cortical neuronal groups. *Proceedings of the National Academy of Sciences* **108**, 5419-5424 (2011).

55 Florez, C. *et al.* In vitro recordings of human neocortical oscillations. *Cerebral Cortex* **25**, 578-597 (2013).

56 Habib, N. *et al.* Massively parallel single-nucleus RNA-seq with DroNc-seq. *Nature methods* **14**, 955 (2017).

57 Mansouri, A., Fallah, A. & Valiante, T. A. Determining surgical candidacy in temporal lobe epilepsy. *Epilepsy research and treatment* **2012** (2012).

58 Kostopoulos, G., Drapeau, C., Avoli, M., Olivier, A. & Villemeure, J. G. Endogenous adenosine can reduce epileptiform activity in the human epileptogenic cortex maintained in vitro. *Neuroscience letters* **106**, 119-124 (1989).

59 Köhling, R. & Avoli, M. Methodological approaches to exploring epileptic disorders in the human brain in vitro. *Journal of neuroscience methods* **155**, 1-19 (2006).

60 Ting, J. T., Daigle, T. L., Chen, Q. & Feng, G. in *Patch-Clamp Methods and Protocols* 221-242 (Springer, 2014).

61 Gouwens, N. W. *et al.* Classification of electrophysiological and morphological neuron types in the mouse visual cortex. *Nature neuroscience* **22**, 1182-1195 (2019).

62 Poorthuis, R. B. *et al.* Rapid neuromodulation of layer 1 interneurons in human neocortex. *Cell reports* **23**, 951-958 (2018).

63 Torres-Gomez, S. *et al.* Changes in the Proportion of Inhibitory Interneuron Types from Sensory to Executive Areas of the Primate Neocortex: Implications for the Origins of Working Memory Representations. *Cerebral Cortex* (2020).

64 Galán, R. F., Ermentrout, G. B. & Urban, N. N. Optimal time scale for spike-time reliability: theory, simulations, and experiments. *Journal of neurophysiology* **99**, 277-283 (2008).

bioRxiv preprint doi: https://doi.org/10.1101/748988; this version posted April 17, 2021. The copyright holder for this preprint (which was not certified by peer review) is the author/funder, who has granted bioRxiv a license to display the preprint in perpetuity. It is made available under aCC-BY-NC-ND 4.0 International license.

65 Neske, G. T. & Connors, B. W. Distinct roles of SOM and VIP interneurons during cortical up states. *Frontiers in neural circuits* **10**, 52 (2016).

Acknowledgements

We are immensely grateful to our neurosurgical patients and their families for consenting to the use of their tissue samples for research. We thank Dr. Gelareh Zadeh and Dr. Mark Bernstein for their assistance in obtaining brain tissue samples and Victoria Barkley and Marjan Rafiee for assistance compiling demographic and chart information. We thank Sara Mahallati and Iliya Weisspapir for assistance in tissue preparation. We thank Brian Kalmbach for helpful conversations that informed our analysis of subthreshold resonance targeting of Layer 3c pyramidal cells. We thank Frances K Skinner, Etay Hay, Wesley Sacher, Dene Ringuette, Xiao Luo, and Jasmine Bell for their critical comments on the manuscript. We thank James Jonkman (Advanced Optical Microscopy Facility, University Health Network) for acquiring the two-photon images. We acknowledge generous support from the Centre for Addiction and Mental Health Discovery Fund, Krembil Brain Institute Fund, National Institute of Health, and Kavli Foundations.

Author Contributions

Conception or design of the experiments: HMC, TAV; Data collection: HMC, LW; Data analysis and interpretation: HMC, ST, SR, FC, TAV; Drafting the article HMC, ST, SR, TAV; Critical revision of the article: HMC, ST, SR, TAV; Final approval of the version to be published: HMC, SR, LW, FC, LZ, PLC, ST, TAV.

Competing Interest

The authors declare no competing interests.

bioRxiv preprint doi: https://doi.org/10.1101/748988; this version posted April 17, 2021. The copyright holder for this preprint (which was not certified by peer review) is the author/funder, who has granted bioRxiv a license to display the preprint in perpetuity. It is made available under aCC-BY-NC-ND 4.0 International license.

Supplementary Information

Diversity amongst human cortical pyramidal neurons revealed via their sag currents and frequency preferences

Homeira Moradi Chameh[1], Scott Rich[1], Lihua Wang[1], Fu-Der Chen[2,3], Liang Zhang[1,4], Peter L. Carlen[1,4,5], Shreejoy J. Tripathy[6,7,8†], Taufik A. Valiante[1,2,5,7,9*†]

[1]Krembil Brain Institute, University Health Network, 60 Leonard Street, Toronto, ON, Canada, M5T2S8. [2]Department of Electrical and Computer Engineering, University of Toronto, 10 king's College Rd, Toronto, ON, Canada, M5S 3G8. [3]Max Planck Institute of Microstructure Physics, Weinberg 2, 06120, Halle, Germany. [4]Departments of Medicine & Physiology, University of Toronto, King's College Circle, Medical Science Building, Toronto, ON, Canada, M5S 1A8. [5]Institute of Biomedical Engineering, University of Toronto, Rosebrugh Building, 164 College Street, Toronto, ON, Canada, M5S 3G9. [6]Krembil Centre for Neuroinformatics, Centre for Addiction and Mental Health, 250 College Street, Toronto, ON, Canada, M5T 1R8. [7]Institute of Medical Sciences, University of Toronto, King's College Circle, Medical Science Building, Toronto, ON, Canada, M5S 1A8. [8]Department of Psychiatry, University of Toronto, 250 College Street, Toronto, ON, Canada, M5T 1R8. [9]Department of Surgery, Division of Neurosurgery, University of Toronto, Stewart Building, 149 College Street, Toronto, ON, Canada. M5T 1P5.

[†]These authors contributed equally.
* taufik.valiante@uhn.ca

bioRxiv preprint doi: https://doi.org/10.1101/748988; this version posted April 17, 2021. The copyright holder for this preprint (which was not certified by peer review) is the author/funder, who has granted bioRxiv a license to display the preprint in perpetuity. It is made available under aCC-BY-NC-ND 4.0 International license.

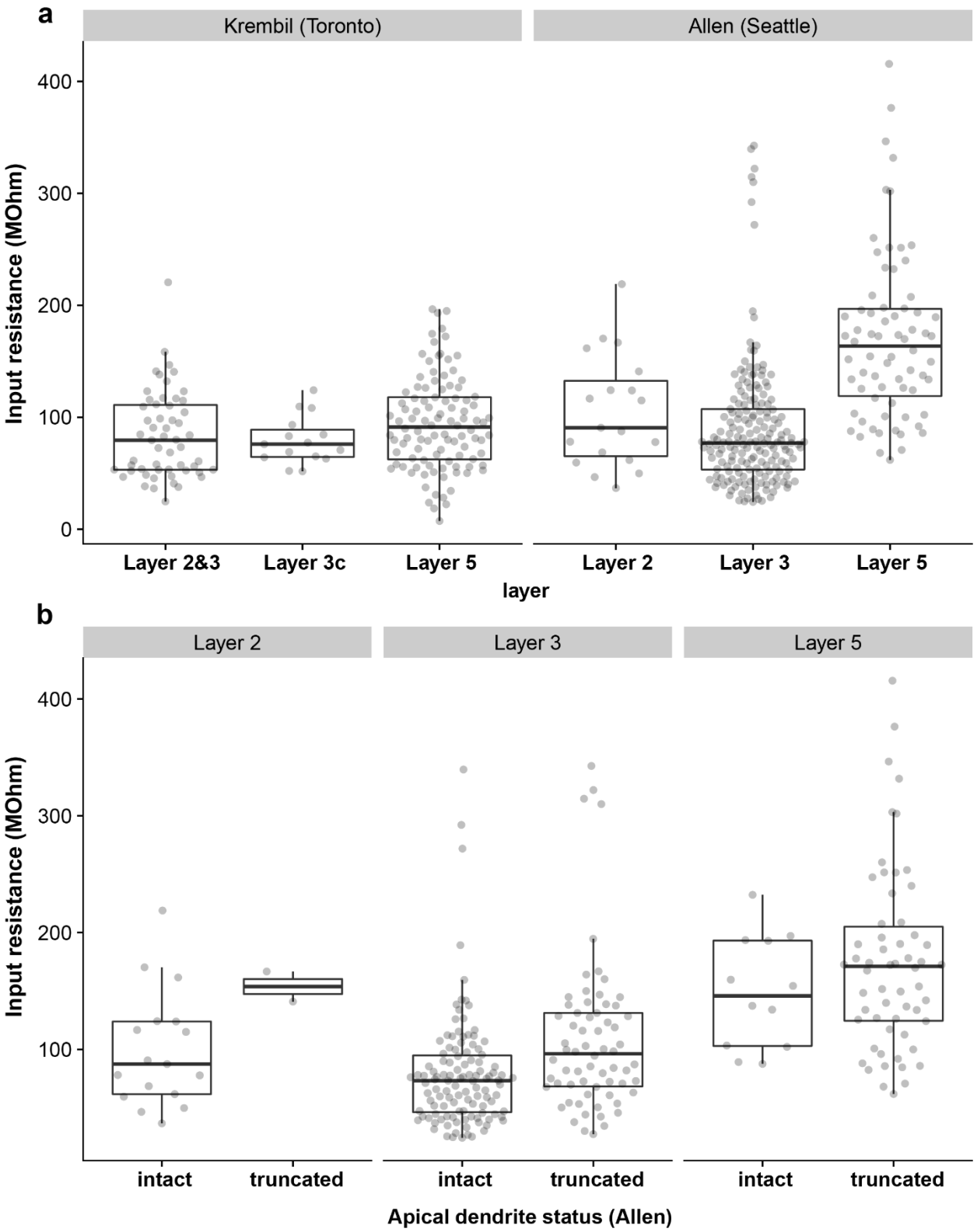

bioRxiv preprint doi: https://doi.org/10.1101/748988; this version posted April 17, 2021. The copyright holder for this preprint (which was not certified by peer review) is the author/funder, who has granted bioRxiv a license to display the preprint in perpetuity. It is made available under aCC-BY-NC-ND 4.0 International license.

Supplementary Figure 1: Comparison of input resistance measurements in human cortical pyramidal cells collected from the Krembil Brain Institute and the Allen Institute. a Input resistance measurements from Krembil Brain Institute cohort (left, n = 56, 15, 105 for L2&3, L3c, L5, respectively) and Allen Institute cohort (right, n = 19, 181, 70 for L2, L3, L5, respectively). Note the trend of increased input resistances in L5 pyramidal cells relative to L2&3 neurons. **b** Same as right panel of a, but data have been grouped by whether the apical dendrite is intact or truncated (L2, n = 17 intact, 2 truncated; L3, 115 intact, 66 truncated; L5, 12 intact, 58 truncated). According to the Allen Institute's documentation, an apical dendrite is "intact" if the entire length of the primary dendrite was contained within the thickness of the slice and "truncated" if the primary dendritic branch was cut off at either slice surface. While dendrite truncation tends to increase input resistances, the overall relationship that input resistances in L2&3 are smaller than in L5 holds for neurons with confirmed intact primary dendrites. Boxplots denote interquartile range and whiskers denote data range excluding outliers. Source data are provided as a Source Data file.

bioRxiv preprint doi: https://doi.org/10.1101/748988; this version posted April 17, 2021. The copyright holder for this preprint (which was not certified by peer review) is the author/funder, who has granted bioRxiv a license to display the preprint in perpetuity. It is made available under aCC-BY-NC-ND 4.0 International license.

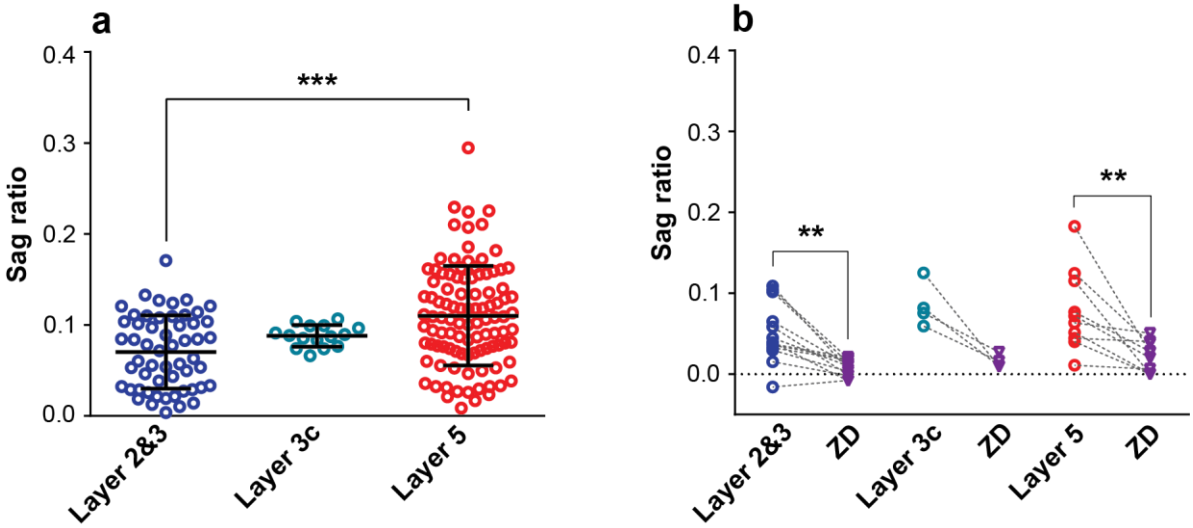

Supplementary Figure 2: Sag differences between cortical layers are robust to normalizing for input resistance differences using the dimensionless sag ratio measure. a Same as Fig 2b, but data are plotted using the sag ratio measure . L5 pyramidal cells had significantly larger sag ratio than L2&3 pyramidal cells ($p<0.0001$ between L2&3 and L5; One-Way ANOVA post hoc with Dunn's multiple comparison test. L2&3: 0.07 ± 0.04 mV, n=55; L3c: 0.08 ± 0.01 mV, n=15; L5: 0.11 ± 0.05 mV, n=103). Data presented as mean±SD **b** Same as Fig 2e, showing bath application of Ih blocker ZD7288 (10 µM) reducing sag ratio in pyramidal cells from both layers (L2&3-ZD: p=0.0005, n=13; L3c-ZD: p=0.1250, n=4; L5-ZD: p=0.0020, n=10; Wilcoxon matched-pairs signed rank test). Source data are provided as a Source Data file.

bioRxiv preprint doi: https://doi.org/10.1101/748988; this version posted April 17, 2021. The copyright holder for this preprint (which was not certified by peer review) is the author/funder, who has granted bioRxiv a license to display the preprint in perpetuity. It is made available under aCC-BY-NC-ND 4.0 International license.

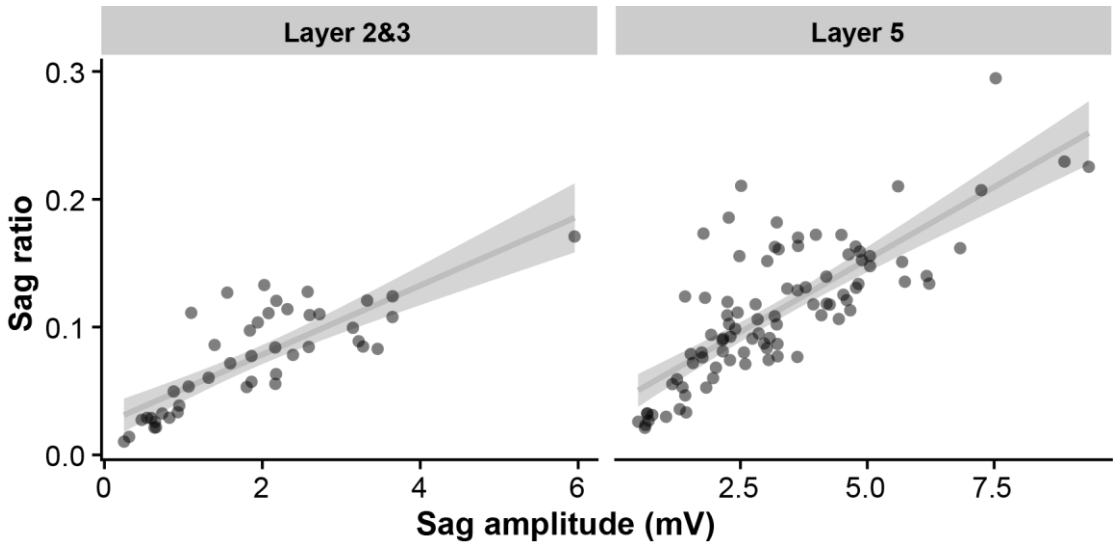

Supplementary Figure 3: Correlation between sag voltage and sag ratio in data from the Krembil Brain Institute cohort. Source data are provided as a Source Data file.

bioRxiv preprint doi: https://doi.org/10.1101/748988; this version posted April 17, 2021. The copyright holder for this preprint (which was not certified by peer review) is the author/funder, who has granted bioRxiv a license to display the preprint in perpetuity. It is made available under aCC-BY-NC-ND 4.0 International license.

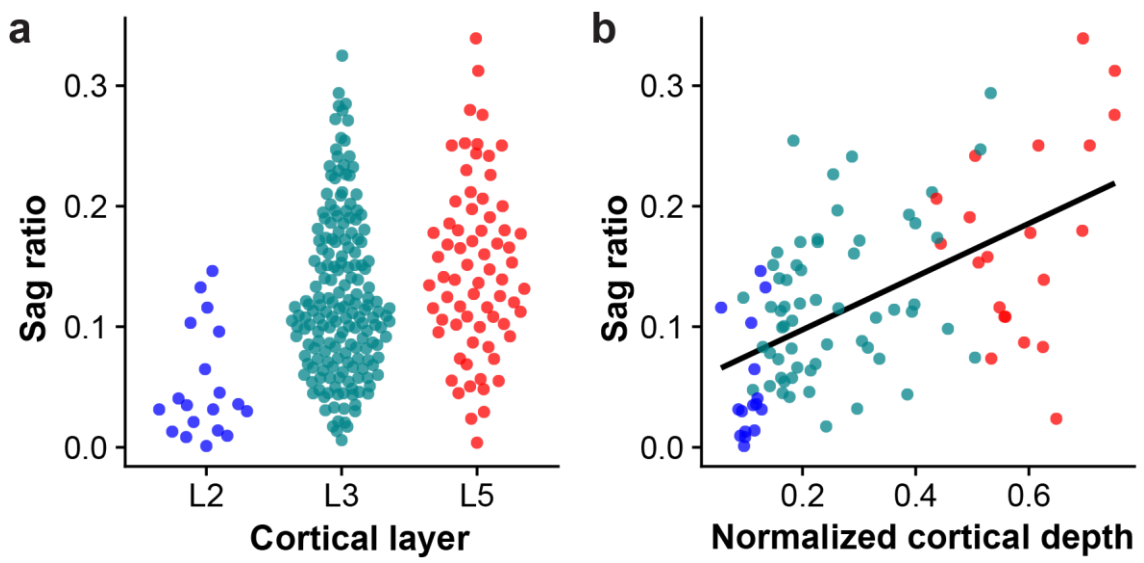

Supplementary Figure 4: Sag ratio measurements in human cortical pyramidal cells collected from the Allen Institute. a Sag ratio measurement collected in each cortical layer (n = 19, 181, 70 for L2, L3, L5, respectively). **b** Sag ratio as a function of normalized cortical depth from the pial surface (n = 16, 59, 21 for L2, L3, L5, respectively). Cells are a subset of those shown in (a) with normalized cortical depth information available. Line indicates best fit line. Source data are provided as a Source Data file.

bioRxiv preprint doi: https://doi.org/10.1101/748988; this version posted April 17, 2021. The copyright holder for this preprint (which was not certified by peer review) is the author/funder, who has granted bioRxiv a license to display the preprint in perpetuity. It is made available under aCC-BY-NC-ND 4.0 International license.

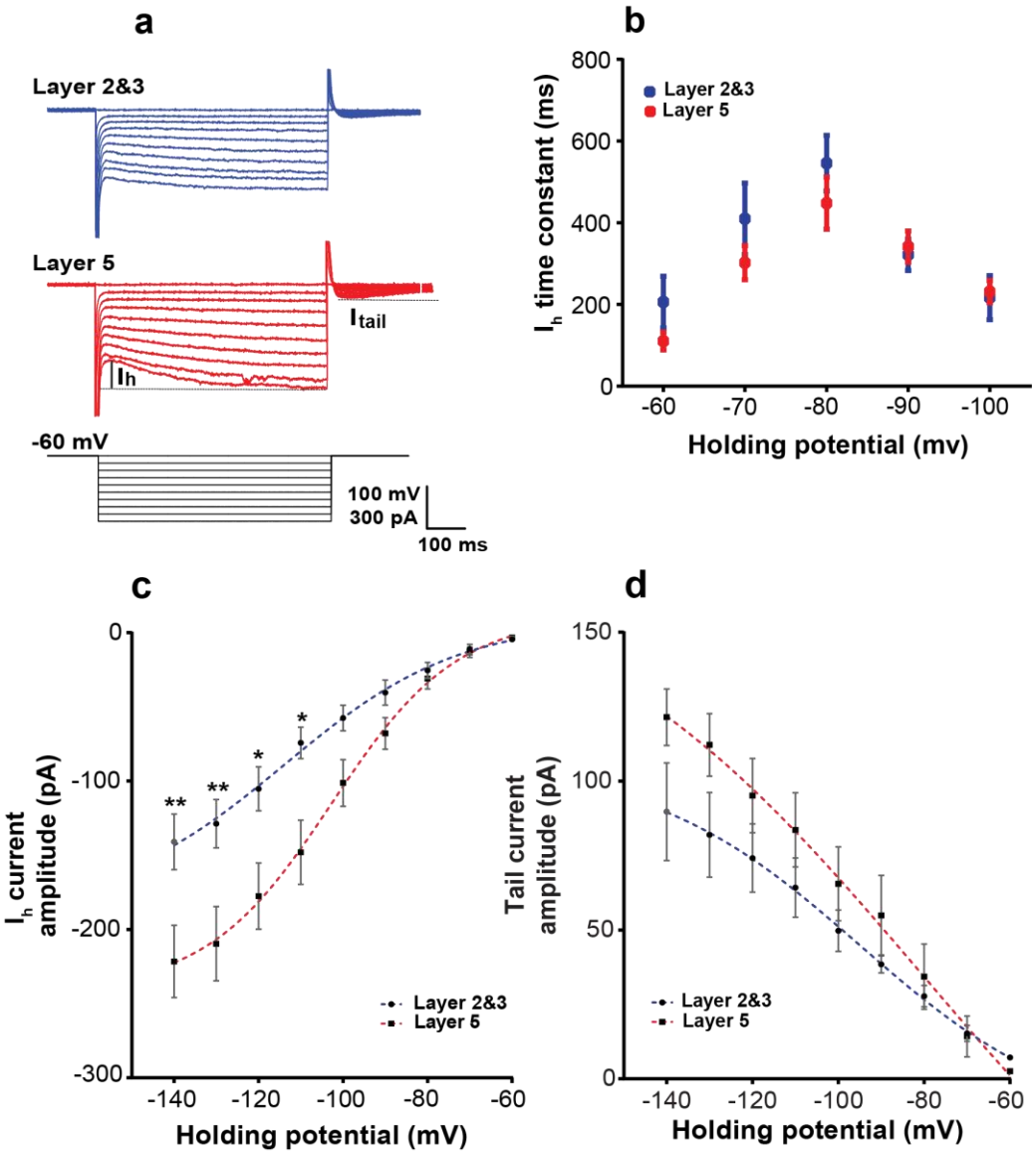

Supplementary Figure 5: The kinetics of I_h are similar between L2&3 and L5 pyramidal cells. a Example voltage-clamp recordings of L2&3 and L5 pyramidal cells. Annotations show calculation of I_h and I_{tail}. **b** Voltage clamp recordings of current show that I_h time constants are similar between L2&3 and L5 pyramidal cells (p≥0.9999;Two-Way ANOVA post hoc with Bonferroni's multiple comparison test, L2&3: n= 6, L5: n=10) . **c** L5 pyramidal cells had significantly larger I_h amplitude compared to L2&3 pyramidal cells (**p=0.0088, * p=0.0265;Two-Way ANOVA post hoc with Bonferroni's multiple comparison test). **d** Quantification of I_{tail} at the end of each holding potential revealed that there was no significant difference between L2&3 and L5 (p≥0.9999;Two-Way ANOVA post hoc with Bonferroni's multiple comparison test). The dashed lines in **c** and **d** indicates the fit to a Boltzmann function. These data suggest that the difference between sag voltages in L2&3 and L5 pyramidal cells are not due to differences in the kinetics of HCN channels. Data presented as mean ±SEM, L2&3: n= 6, L5: n=10). Source data are provided as a Source Data file.

bioRxiv preprint doi: https://doi.org/10.1101/748988; this version posted April 17, 2021. The copyright holder for this preprint (which was not certified by peer review) is the author/funder, who has granted bioRxiv a license to display the preprint in perpetuity. It is made available under aCC-BY-NC-ND 4.0 International license.

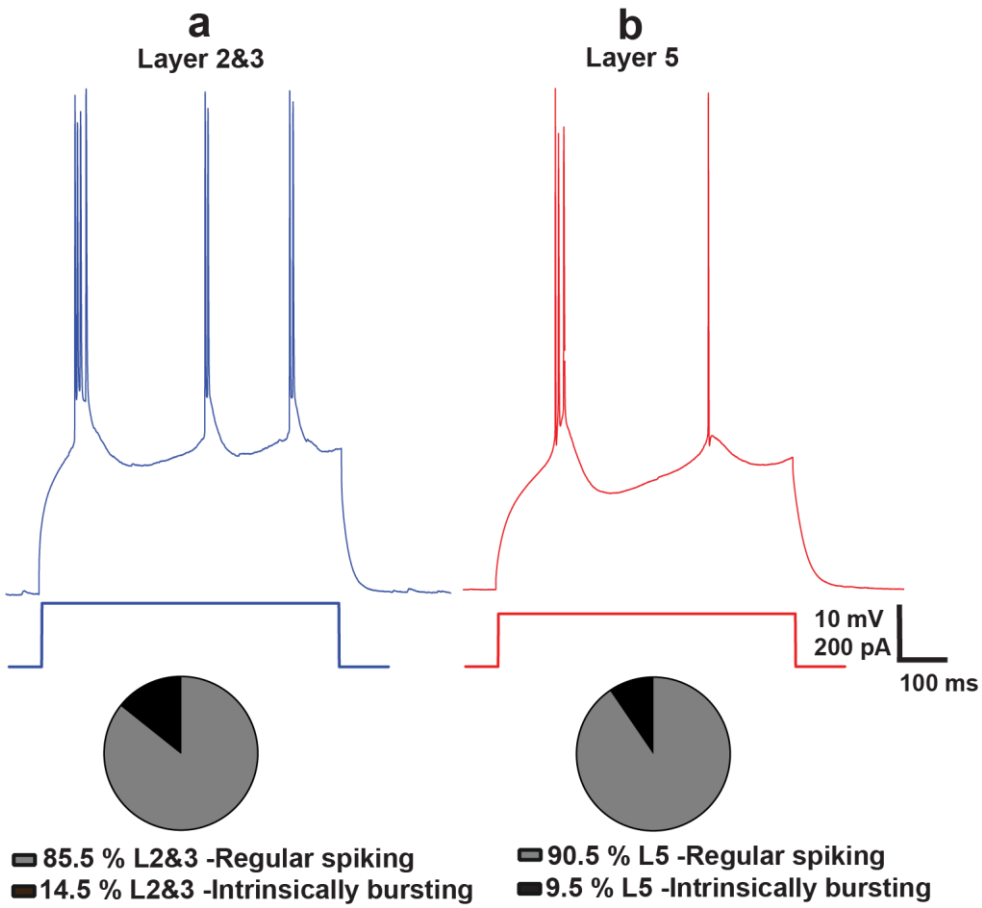

Supplementary Figure 6: Distribution of different firing patterns across L2&3 and L5 pyramidal cells. a,b Example voltage traces of intrinsically bursting neurons at rheobase. L2&3 (a) and L5 (b) pyramidal cells tend to have more regular spiking than intrinsically bursting neurons.The percentage of intrinsically bursting neurons recorded in L2&3 was slightly higher than L5. Source data are provided as a Source Data file.

bioRxiv preprint doi: https://doi.org/10.1101/748988; this version posted April 17, 2021. The copyright holder for this preprint (which was not certified by peer review) is the author/funder, who has granted bioRxiv a license to display the preprint in perpetuity. It is made available under aCC-BY-NC-ND 4.0 International license.

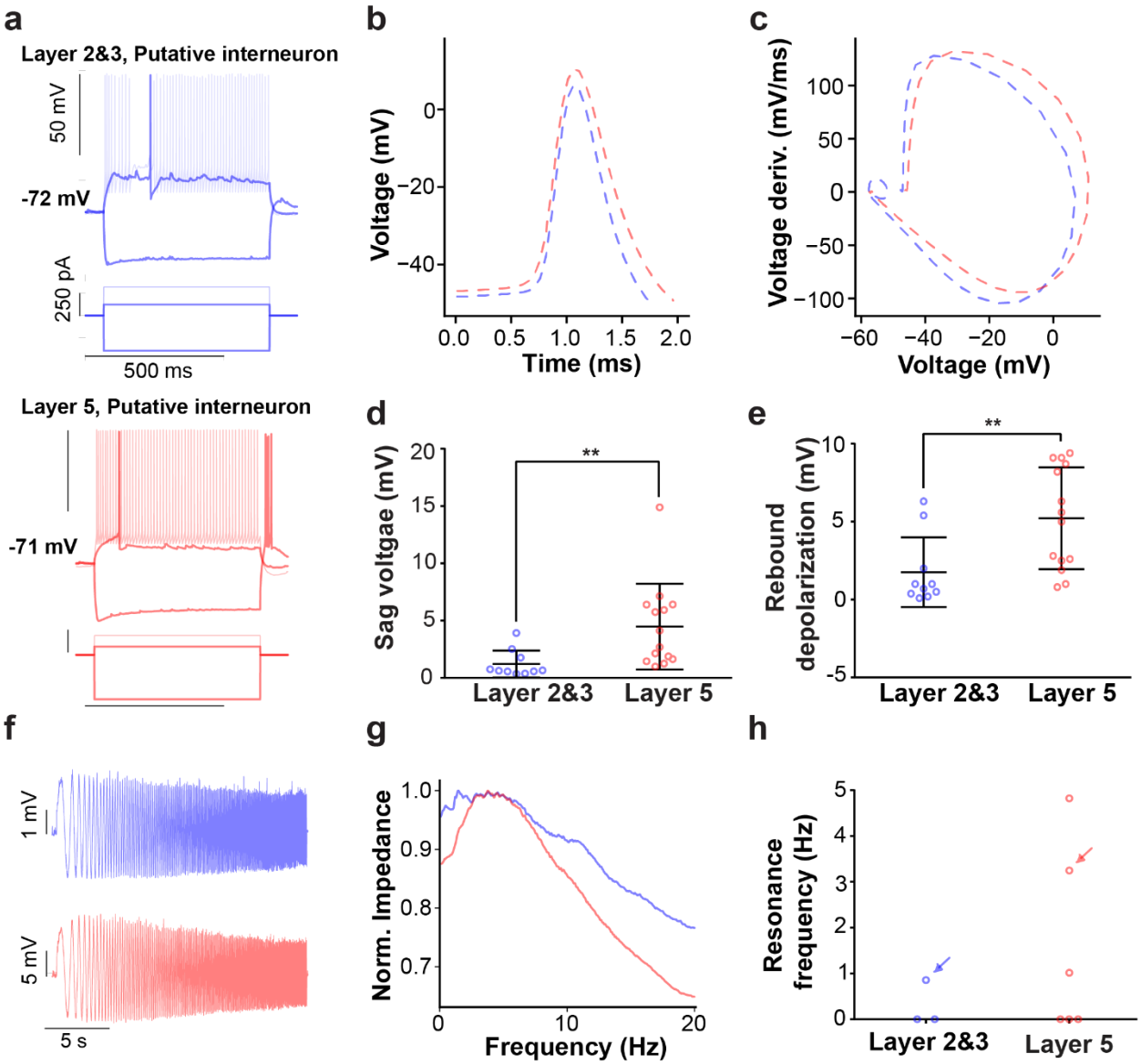

Supplementary Figure 7. Electrophysiological and subthreshold resonance properties of putative interneurons recorded in L2&3 and L5. a Example voltage responses and current steps for an example putative interneuron from L2&3 (top) and L5 (bottom). **b,c** Action potential waveform (b) and action potential phase plot (c) averaged over recorded putative interneurons in L2&3 (blue) and L5 (red). **d,e** Sag amplitude (p= 0.0012; two-sided t-test, Mann-Whitney, L2&3: 1.2 ± 1.1 mV, n=10; L5: 4.5± 3.7 mV, n=14) (d) and post-hyperpolarization rebound depolarization amplitude (p= 0.0032; two-sided t-test, Mann-Whitney, L2&3: 1.7 ± 2.2 mV, n=10; L5: 5.2± 3.2 mV, n=14) (e) reveals greater amounts of sag and rebound depolarization amplitude in L5 putative interneurons compared to L2&3. **f,g** Example subthreshold voltage responses (f) and normalized impedance (g) following ZAP current injection for example neurons shown in **a**. **h** Subthreshold resonance frequencies show a trend for more subthreshold resonance in L5. Arrows indicate neurons highlighted in **f**. Source data are provided as a Source Data file.

bioRxiv preprint doi: https://doi.org/10.1101/748988; this version posted April 17, 2021. The copyright holder for this preprint (which was not certified by peer review) is the author/funder, who has granted bioRxiv a license to display the preprint in perpetuity. It is made available under aCC-BY-NC-ND 4.0 International license.

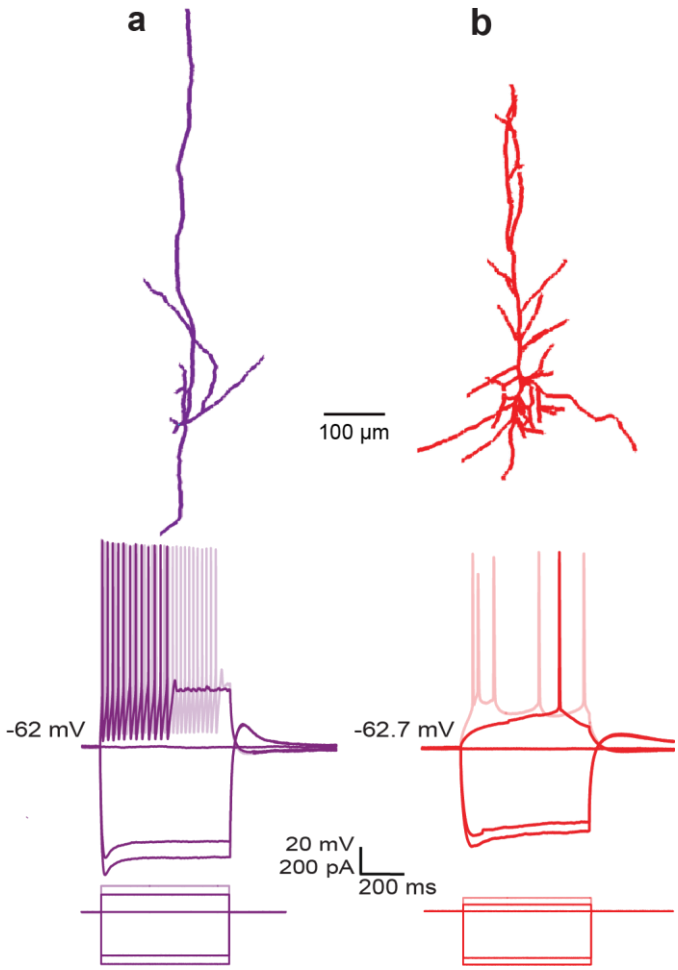

Supplementary Figure 8: Morphological evidence for interneuron sampling. **a** Morphological reconstruction and firing pattern following hyperpolarizing and depolarizing current injections for a putative interneuron; 2100 µm below pia. **b** Morphological reconstruction from a confirmed pyramidal cell (cell f in Figure 1) and related firing pattern following hyperpolarizing and depolarizing current injections; 1800 µm below pia.

bioRxiv preprint doi: https://doi.org/10.1101/748988; this version posted April 17, 2021. The copyright holder for this preprint (which was not certified by peer review) is the author/funder, who has granted bioRxiv a license to display the preprint in perpetuity. It is made available under aCC-BY-NC-ND 4.0 International license.

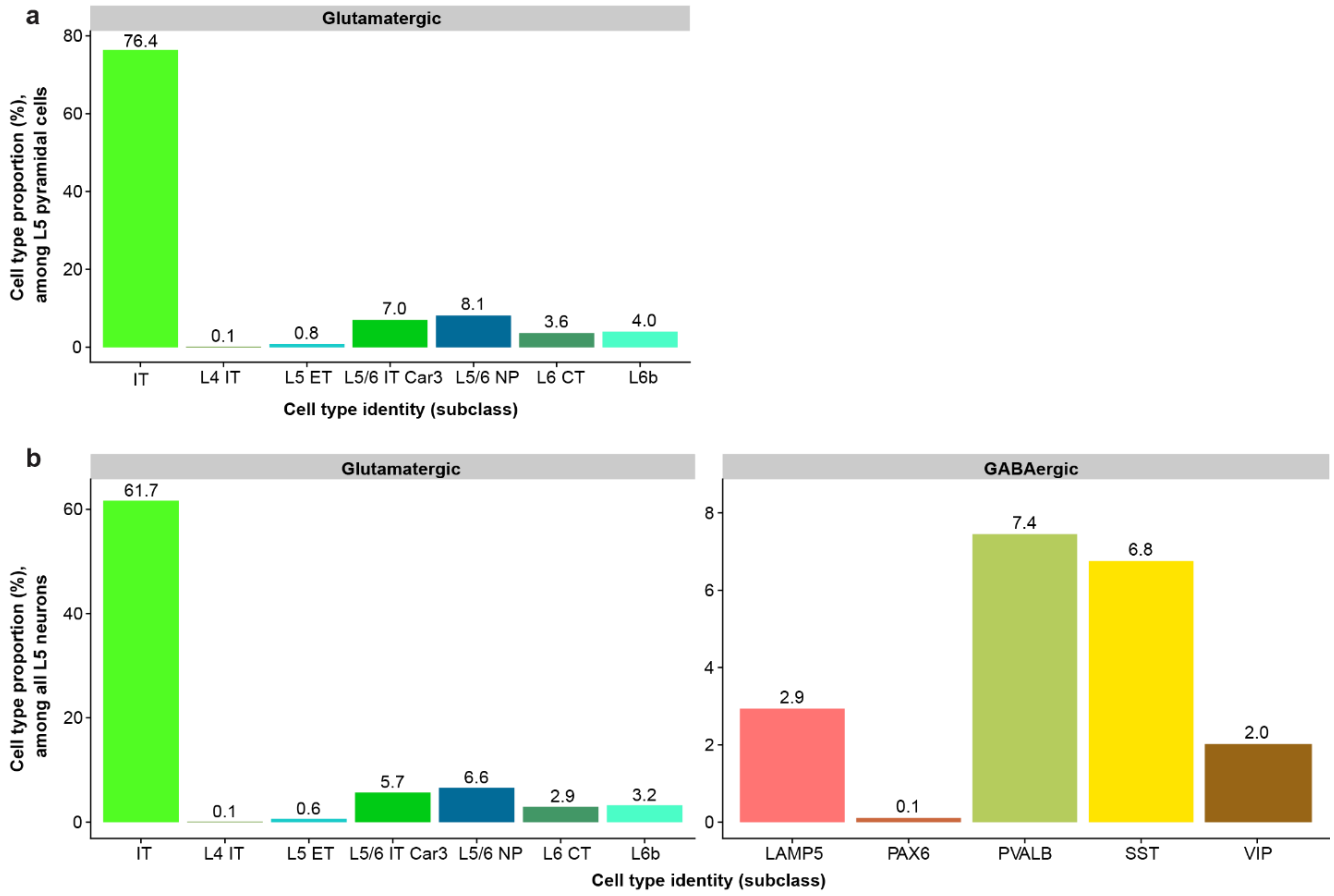

Supplementary Figure 9: Cell type proportions and in human MTG Layer 5 based on single-nucleus RNAseq reference data. Data are replotted from Hodge et.al.[1], based on cortical layer-specific tissue dissections . **a.** Cell type proportions among sampled excitatory (i.e., Glutamatergic) nuclei in L5 (n = 2200 cells total). X-axis denotes cell type labels, annotated to the "subclass" cell type resolution in Hodge et al, 2019. Label "L5 ET" denotes extra-telencephalic projecting cells and "IT" denotes intra-telencephalic projecting cells (identified through transcriptomic similarity and homology to the mouse). **b.** Same as a, but for y-axis denotes cell type proportions relative to all neurons sampled in L5 (n = 2725 cells total). Source data are provided as a Source Data file.

bioRxiv preprint doi: https://doi.org/10.1101/748988; this version posted April 17, 2021. The copyright holder for this preprint (which was not certified by peer review) is the author/funder, who has granted bioRxiv a license to display the preprint in perpetuity. It is made available under aCC-BY-NC-ND 4.0 International license.

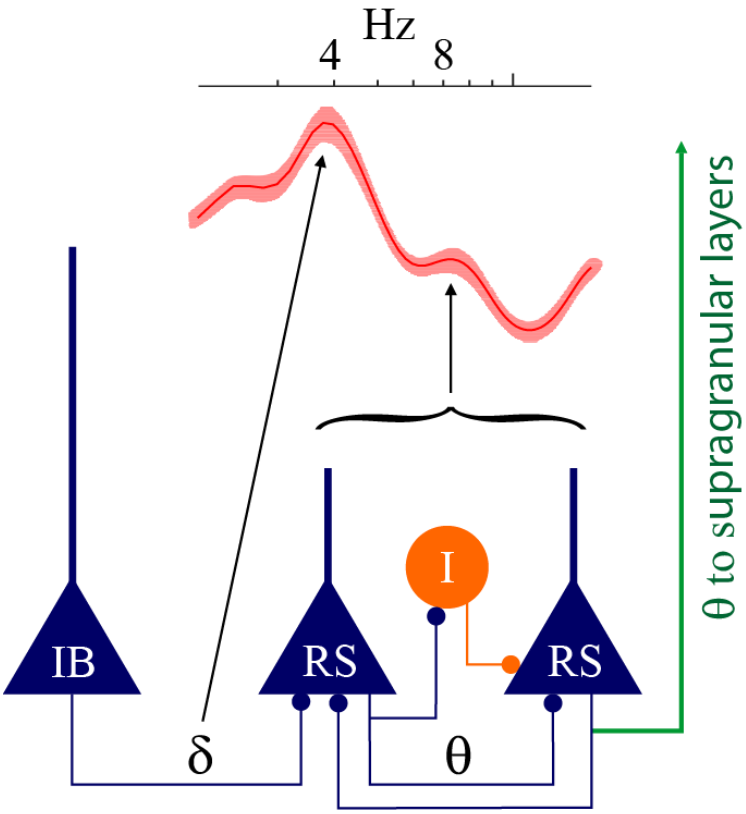

Supplementary Figure 10: Structural circuit motif for L5 theta oscillations. Delta frequency output from intrinsically bursting (IB)[2] neurons is well tracked by regular spiking (RS) neurons that have a peak in G(f) (red) (see Figure 5b in main text) within the delta frequency range. In contrast with IB neurons, RS neurons are poorly adapting, have steep f-I curves, and low rheobase discharge at theta frequency[2]. RS cells drive local circuits at theta frequency range including other RS neurons that track theta well, quantified by the peak at ~8Hz in *G(f)*. Interneurons amplify local activity through rebound excitation (I; orange; see Supplementary Figure 7) in human circuits that are predisposed to reverberant activity[3].

Supplementary references

1 Hodge, R. D. *et al.* Conserved cell types with divergent features in human versus mouse cortex. *Nature* **573**, 61-68 (2019).

2 Carracedo, L. M. *et al.* A neocortical delta rhythm facilitates reciprocal interlaminar interactions via nested theta rhythms. *Journal of Neuroscience* **33**, 10750-10761 (2013).

3 Molnár, G. *et al.* Complex events initiated by individual spikes in the human cerebral cortex. *PLoS biology* **6**, e222 (2008).